

Observations of planetary waves and nonmigrating tides by the Mars Climate Sounder

Scott D. Guzewich,¹ Elsayed R. Talaat,² and Darryn W. Waugh¹

Received 9 August 2011; revised 20 January 2012; accepted 9 February 2012; published 27 March 2012.

[1] Temperature profiles from the Mars Reconnaissance Orbiter's (MRO) Mars Climate Sounder (MCS) indicate the presence of several types of stationary planetary waves and nonmigrating thermal tides in the Martian atmosphere. We analyze 35 months of MCS data to identify the dominant waves. With the contribution of the zonal mean and migrating tides removed, the temperature perturbations remaining are due to planetary waves, nonmigrating tides, and topographic and surface albedo/thermal inertia effects. We characterize waves with satellite-relative wave numbers 1 through 4 in the Martian middle atmosphere (40–80 km). In tropical latitudes, eastward propagating diurnal Kelvin waves are the dominant component observed in the satellite-relative wave number 2 through 4 fields; we identify these as diurnal Kelvin waves 1 through 3, respectively. The Kelvin waves have very long vertical wavelengths and amplitudes of 1–3 K. This is the first unambiguous detection of diurnal Kelvin wave 3. We also identify the zonally symmetric diurnal tide and an eastward propagating semidiurnal wave 1 tide, possibly the semidiurnal Kelvin wave 1. Stationary planetary waves with wave numbers 1 and 2 produce 5–10 K amplitudes in the middle and high latitudes of both hemispheres.

Citation: Guzewich, S. D., E. R. Talaat, and D. W. Waugh (2012), Observations of planetary waves and nonmigrating tides by the Mars Climate Sounder, *J. Geophys. Res.*, 117, E03010, doi:10.1029/2011JE003924.

1. Introduction

[2] Solar heating of the Martian atmosphere and surface drives atmospheric wave motions including global-scale inertia-gravity waves known as thermal tides and stationary planetary waves. Classification of tides is typically divided into migrating and nonmigrating groups. The migrating tides are westward traveling Sun-synchronous waves that are forced by zonally uniform solar heating [Chapman and Lindzen, 1970]. Nonmigrating tides are not Sun synchronous, and can be westward or eastward propagating with varying wave numbers at periods that are integer fractions of a day [e.g., Talaat and Lieberman, 1999]. Longitudinal variations in heating due to, for example: topography, surface thermal inertia changes and variable atmospheric dust and water ice concentrations can excite nonmigrating tides on Mars [Zurek, 1976]. Theory and global circulation models (GCM) predict that Mars' predominantly zonal wave number 2 ($s = 2$) topography will generate nonmigrating tides, with the eastward propagating diurnal Kelvin waves most prominent [Wilson and Hamilton, 1996]. The diurnal Kelvin wave is near resonance in Mars' atmosphere [Zurek, 1976], potentially creating large amplitudes as shown in modeling by Wilson and Hamilton [1996] and in Viking

lander surface pressure observations. Stationary waves are also intimately linked to topographic relief and are forced by airflow over terrain. Suitable wind profiles allow them to propagate vertically and transport heat poleward.

[3] Tides and stationary waves in the Martian atmosphere have been observed in surface air pressure and wind records of the Viking landers and in the atmospheric thermal data from Mariner 9 the Viking orbiters and Mars Global Surveyor (MGS) missions [Conrath, 1976, 1981; Hess *et al.*, 1977; Martin, 1981; Zurek and Leovy, 1981; Banfield *et al.*, 2000; Wilson, 2000; Banfield *et al.*, 2003; Hinson *et al.*, 2003, 2008]. MGS also observed the effects of tides and planetary waves in density variations during its extended aerobraking campaign [Forbes *et al.*, 2002; Wilson, 2002; Withers *et al.*, 2003] and in radio occultations (RO) [Bougher *et al.*, 2001; Hinson *et al.*, 2003; Cahoy *et al.*, 2006]. Specific tides previously observed include the migrating diurnal and semidiurnal tides, diurnal Kelvin waves with wave numbers 1 ($s = 1$) and 2 ($s = 2$) (DK1 and DK2 hereafter), semidiurnal Kelvin $s = 2$ (SK2), and an eastward propagating semidiurnal $s = 1$ (likely the semidiurnal Kelvin $s = 1$ (SK1)). Stationary waves with $s = 1$ and $s = 2$ have been identified at the high latitudes of both hemispheres. MCS has been employed to study the migrating diurnal tide [Lee *et al.*, 2009] and zonal mean temperature structures [Lee *et al.*, 2009; McCleese *et al.*, 2010; Heavens *et al.*, 2011a]. The availability of data from the MCS instrument onboard MRO, which measures temperature profiles from the surface to 80 km altitude with 5 km vertical resolution and near global coverage [McCleese *et al.*,

¹Department of Earth and Planetary Sciences, Johns Hopkins University, Baltimore, Maryland, USA.

²Johns Hopkins University Applied Physics Laboratory, Laurel, Maryland, USA.

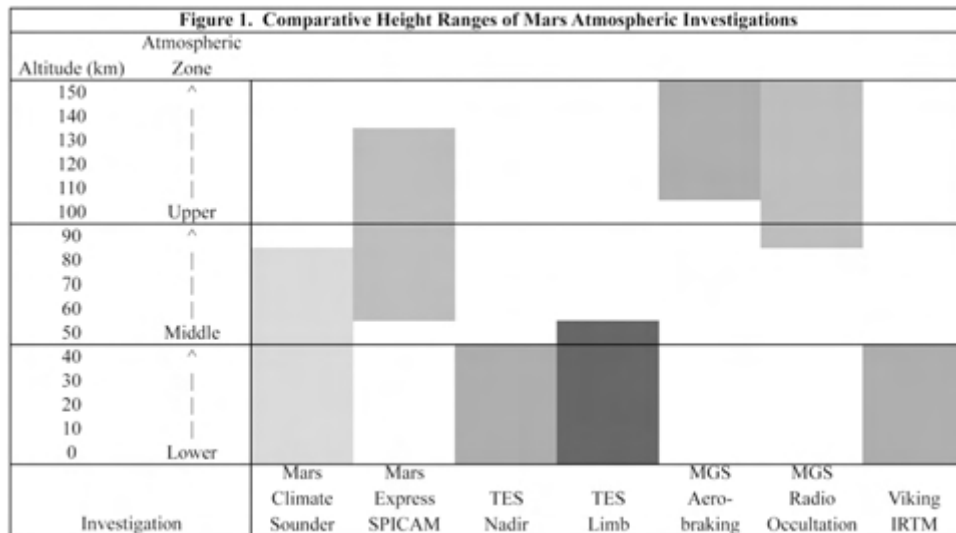


Figure 1. Altitude ranges in the Martian atmosphere observed by MCS and other past atmospheric investigations. MCS has the broadest coverage in the Martian middle atmosphere to date. Atmospheric zones are from Zurek *et al.* [1992]. MCS is from McCleese *et al.* [2007]. SPICAM is from Forget *et al.* [2009]. TES Nadir is from Banfield *et al.* [2003]. TES Limb is from Smith *et al.* [2001]. MGS Aerobraking is from Keating *et al.* [1998]. MGS Radio Occultation is from Bougher *et al.* [2001]. Viking IRTM is from Wilson and Richardson [2000].

2007, 2010], provides an opportunity to examine tides throughout the Martian lower and middle atmosphere. Figure 1 compares the vertical range of MCS measurements with previous investigations.

[4] Here we examine the structure of nonmigrating tides and stationary waves from the surface to 80 km using 35 months of MCS data. This links the previously separate lower-atmosphere observations (e.g., from MGS Thermal Emission Spectrometer (TES)) with the upper atmosphere and thermosphere (e.g., from MGS RO). We observe and characterize waves from the surface to 80 km altitude and report the first unambiguous detections of diurnal Kelvin wave 3 (DK3). Section 2 describes the data used and the analysis methods. Section 3 discusses the results and identifies the observed waves. Section 4 provides conclusions.

2. Data and Analysis

[5] MCS is a limb-scanning infrared radiometer launched in 2005 aboard MRO. Its primary science mission began in late September 2006 ($L_s = 110$). Technical information about the MCS instrument is described by McCleese *et al.* [2007]. Pressure is retrieved simultaneously and used as the vertical coordinate in reporting the data. Vertical resolution is 5 km with horizontal resolution ranging from 150–300 km, depending on altitude. Latitude and longitude reported on MCS data files in the Planetary Data System represent the approximate limb tangent points of the profile [Kleinböhl *et al.*, 2009].

[6] The uncertainty in the temperature measurements are 0.4 K (0.25% assuming average temperatures) from 5 to 300 Pa. Closer to the surface, where the atmosphere is more opaque, the errors are 0.5–3 K (0.5–3%). Above 5 Pa, the errors steadily increase, reaching 1 K at 1.5 Pa, 2 K near 0.6 Pa, 5 K near 0.17 Pa and 10 K near 0.06 Pa. These higher

errors are still <10% of average temperatures, and do not exceed 10% until 0.03 Pa. Standard deviations of the error are approximately the same magnitude as the error themselves. Our analysis involved combining morning and afternoon temperatures, each with independent errors, so the errors are added in quadrature. Therefore, the percentage errors in our derived wave amplitudes are slightly less than the original instrument errors for a given location.

[7] This study uses 35 months (September 2006 to August 2009 or $L_s = 110$ of Mars year 28 through $L_s = 330$ of Mars year 29, with August 2007 missing) of version 1 derived data records from MCS, with 1 million profiles analyzed. MRO follows a near-polar Sun-synchronous orbit with 03:00 and 15:00 local solar time (LST) equatorial overpasses. This orbit, with fixed LST overpasses, is non-optimal for detecting waves that are functions of LST. A sampling frequency of 2 samples per sol implies a Nyquist frequency for observable waves of 1 cycle per sol (the diurnal frequency), and aliases higher-frequency waves to those below the Nyquist limit. The waves observed by the satellite are therefore in a satellite-relative coordinate frame that aliases waves to higher or lower wave numbers depending on direction of propagation [Salby, 1982].

[8] Following the method of Lee *et al.* [2009], data were selected to fall within 2 h of MRO's 03:00 and 15:00 LST Sun-synchronous orbit, thus eliminating most data poleward of 70° . High water ice opacities in the tropics, particularly during the aphelion cloud belt season, also caused many profiles to be irretrievable. Data were divided into 12 “months” corresponding to 30 of solar longitude (centered on 0, 30, etc.) and binned into 5 15 latitude-longitude bins. Periods centered on $L_s = 0$ to 90 included data from one Martian year while periods centered on $L_s = 120$ to 330 averaged data from two Martian years. Data were also combined seasonally through 90 of solar longitude to verify

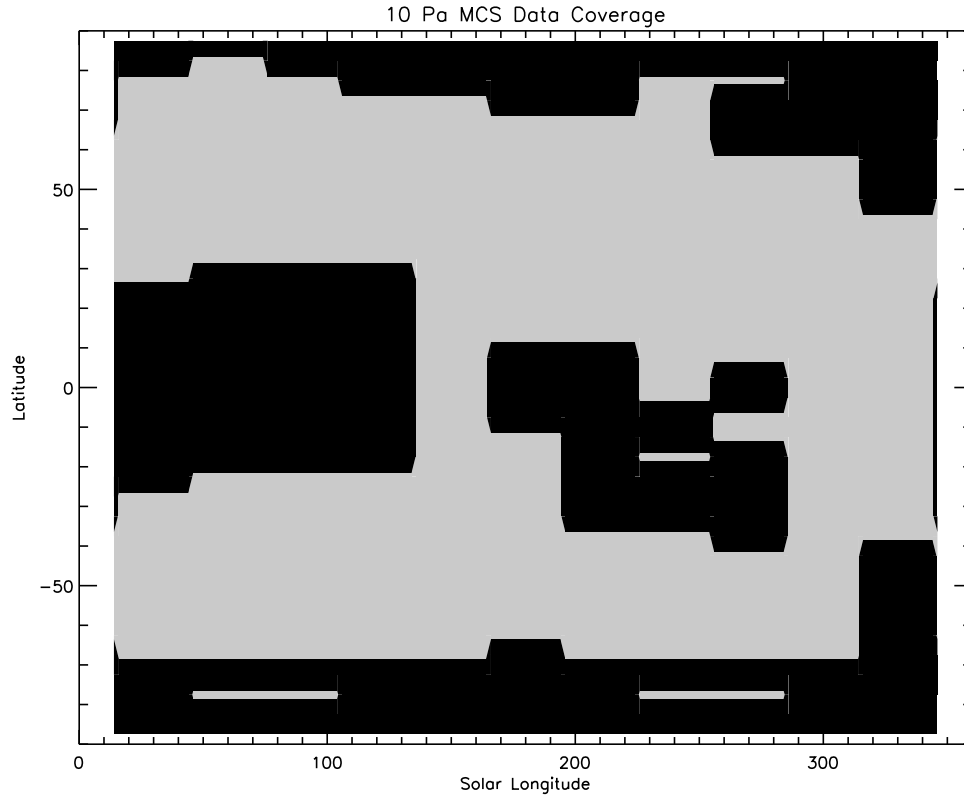


Figure 2. Latitudinal coverage of MCS data used in this study at the 10 Pa pressure level. Areas with available data are shown in gray.

that observed features were persistent with longer time averaging, as discussed in sections 3.4, 3.6, and 3.8. Refer to Figure 2 to see latitudinal coverage of the data through the Martian year.

[9] We assume a wave that is a function of longitude (λ), latitude (φ), pressure (p) and time (t) has the following form:

$$T(\lambda, \varphi, p, t) = \Sigma A_{s,\sigma} \cos(s\lambda + \sigma t + \delta) \quad (1)$$

where s is the zonal wave number, λ is longitude, σ is frequency (units of sol^{-1}) and δ is the phase offset. By shifting our frame of reference to one of fixed local time and neglecting the pressure dependence, equation (1) can be simplified to:

$$T(\lambda, t_{\text{LST}}) = \Sigma A_{s,\sigma} \cos[(s - \sigma)\lambda + \sigma t_{\text{LST}} + \delta] \quad (2)$$

where t_{LST} is local time. Negative (positive) σ implies eastward (westward) propagation. Waves observed in the satellite reference frame (i.e., fixed local time) at satellite-relative wave number m can be attributed to any combination of aliased waves such that $m = |s - \sigma|$ [Forbes and Hagan, 2000; Wilson, 2000; Lee et al., 2009]. An example being that a wave number 2 ($m = 2$) wave can be due to the presence of the following wave forms: $T_{2,0}$ (stationary wave 2), $T_{3,1}$ (westward diurnal wave 3), $T_{1,-1}$ (eastward diurnal wave 1), etc. According to classical tidal theory, any particular s and σ set includes multiple Hough modes each with a characteristic vertical and latitudinal structure. See Figure 3 for plots of the normalized temperature response to particular tidal modes discussed in section 3.

[10] The data are analyzed by examining fields of average and difference temperature plots (as in the work of Lieberman [1991], Lee et al. [2009], Banfield et al. [2003], and others) as follows:

$$\text{T-average} = (T_{3\text{pm}} + T_{3\text{am}})/2 \quad (3)$$

$$\text{T-difference} = (T_{3\text{pm}} - T_{3\text{am}})/2 \quad (4)$$

Returning to equation (2), it becomes obvious that there is an offset of π radians between 15:00 and 03:00 local solar time (LST). This implies that the solution to equation (2) is the same at each time with the offset of $\sigma\pi$ within the cosine argument. This can be restructured to indicate a dependence of $(-1)^\sigma$ between the two temperatures. Then equations can be derived for T-average and T-difference from the restructured equation (2) (and noting that longitude and local time are equivalent here).

$$\text{T-average}(\lambda) = 1/2 * \Sigma (1 + (-1)^\sigma) A_{s,\sigma} \cos[(s - \sigma)\lambda + \sigma (3 \text{ pm}) + \delta] \quad (5)$$

$$\text{T-difference}(\lambda) = 1/2 * \Sigma (1 - (-1)^\sigma) A_{s,\sigma} \cos[(s - \sigma)\lambda + \sigma (3 \text{ pm}) + \delta] \quad (6)$$

It is now obvious that only terms with even σ will appear in T-average and only odd σ terms will appear in T-difference. This limits the number of components that contribute to a T-average or T-difference field with a satellite-relative

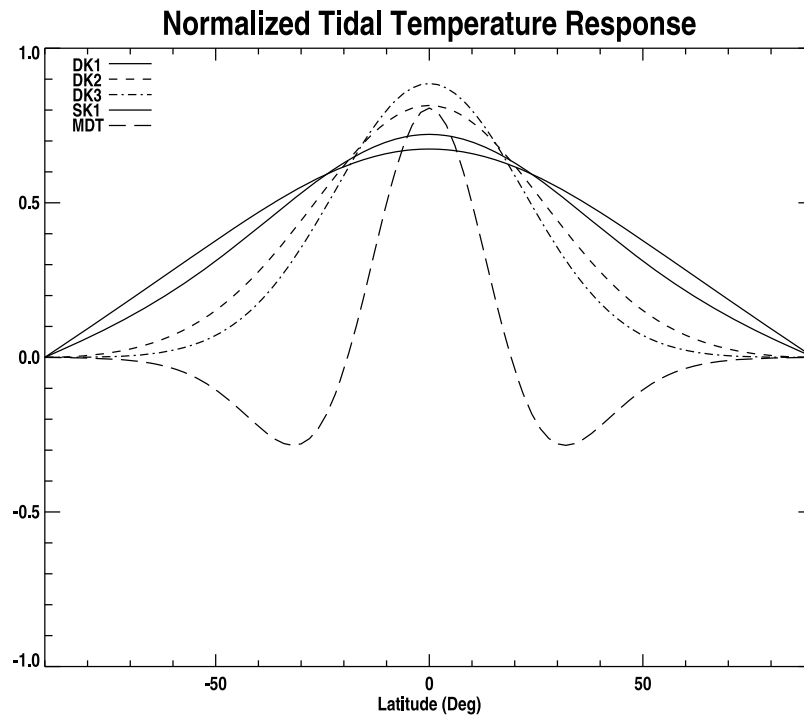


Figure 3. Latitudinal structure of the normalized tidal temperature response of Hough modes contributing to the diurnal Kelvin wave 1 (DK1), diurnal Kelvin wave 2 (DK2), diurnal Kelvin wave 3 (DK3), semidiurnal Kelvin wave 1 (SK1), and the migrating diurnal tide (MDT). Each tide is normalized to itself, and relative amplitudes between tides should not be compared.

specific wave number, m [Forbes and Hagan, 2000; Wilson, 2000, 2002; Banfield, et al., 2003; Lee et al., 2009]. See Table 1 for expected waves that contribute to a given field.

[11] Oberheide et al. [2002] present a method to “de-alias” a field consisting of a superposition of two waves (e.g., $m = 2$ T-difference field) and provide amplitudes and phases of each wave [see also Lieberman et al., 2004]. This method was tested using artificial data (where the exact form of the two waves were known) as well as the Mars data. In both cases the method did not yield robust results. The method produces weaker amplitudes than the true (for the artificial data) or expected (for Mars data) amplitudes, and the summed amplitudes did not match the total amplitude. At best, the application of this method appears to confirm our expectation for the proportional contribution of each tide to the aliased temperature amplitudes in a field. For these reasons, the results are not presented here.

[12] Our analysis proceeded by removing the zonal mean for each latitude bin and altitude, thereby also removing the migrating tide and zonal mean signature in order to examine nonmigrating and stationary wavefields [e.g., Talaat and Lieberman, 1999]. The remaining monthly composites represent satellite-relative (asynoptic) coordinates as defined by Salby [1982]. As a result, eastward (westward) propagating waves are Doppler-shifted one wave number higher (lower).

[13] Finally, the amplitude and phase of the composite temperatures fields were calculated using discrete Fourier transforms (DFT) in longitude. Increasing (decreasing) phase of the maximum with height suggests eastward (westward) propagation of a surface or lower-atmosphere forced, vertically propagating inertia-gravity wave. Although each

Table 1. Wave Modes That Contribute to Each Satellite-Relative Wave Number

Field Type	S	σ	Comments
<i>Satellite-Relative Wave Number 1 (m)</i>			
Average	1	0	stationary wave
	1	2	
	3	2	
Difference	0	1	zonally symmetric diurnal tide
	2	1	
<i>Satellite-Relative Wave Number 2 (m)</i>			
Average	2	0	stationary wave
	0	2	zonally symmetric semidiurnal tide
	4	2	
Difference	1	1	includes diurnal Kelvin wave 1
	3	1	
<i>Satellite-Relative Wave Number 3 (m)</i>			
Average	3	0	stationary wave
	1	2	includes semidiurnal Kelvin wave 1
	5	2	
Difference	2	1	includes diurnal Kelvin wave 2
	4	1	
<i>Satellite-Relative Wave Number 4 (m)</i>			
Average	4	0	stationary wave
	2	2	
	6	2	
Difference	3	1	includes diurnal Kelvin wave 3
	5	1	

average and difference field below consists of multiple aliased waves, separating those fields explicitly into individual waves (or even separating into eastward and westward propagating fields) is not possible. From the Sun-synchronous viewpoint, these waves are degenerate with respect to one another. To determine which wave is dominant in a particular field, observable features such as vertical wavelength and phase are utilized. For example, in the $m = 2-4$ T-difference fields, we expect eastward propagating Kelvin waves to be aliased with westward propagating diurnal nonmigrating tides. The former have very deep vertical wavelengths, while the latter have much shorter vertical wavelengths. The $m = 2-4$ T-difference fields all exhibit very deep vertical wavelengths and eastward propagation, similar to those of Kelvin waves (as expected from tidal theory). Similarly, for the $m = 1-2$ T-average fields, in addition to the vertical wavelength criteria, high-temperature amplitudes are seen at low altitudes in middle and high latitudes near the expected location of the polar jet. This matches theoretical expectations of planetary waves, whereas tides would be more prominent in tropical latitudes and at higher altitudes. In conjunction with classical tidal theory and previously published observations and modeling results, these criteria allow us to classify a particular wave as dominant in each field and attribute the bulk of the temperature amplitude to that wave.

3. Results

[14] We first identified the migrating diurnal tide ($s = 1$, $\sigma = 1$) throughout the Martian year by studying the zonal mean ($m = 0$) T-difference field. The pattern identified by Lee *et al.* [2009, Figure 5] in MCS data for the first half of a Martian year generally holds for the second half as well, with clear patterns of alternating minima and maxima in temperatures through a vertical column. This is a classic signature of the migrating thermal tide with strongest temperature amplitudes (of greater than 10 K at times) seen near the equator. The simulations Lee *et al.* [2009, Figure 10] conducted using the MarsWRF general circulation model to identify the migrating diurnal tide and extend their analysis to parts of the Martian year not yet observed by their publication date match our analysis with more recent MCS data very well (Figure 4). MarsWRF is run with a prescribed dust concentration based on climatology [Richardson *et al.*, 2007]. McCleese *et al.* [2010] show that much of Mars years 28 and 29 exhibited normal dust opacity as understood from previous studies, therefore the dust forcing used in Lee *et al.*'s [2009] MarsWRF runs was consistent with MCS observations. The relatively weak global dust storm that occurred in July 2007 ($L_s = 270$) resulted in most MCS profiles to be irretrievable and thus does not significantly contaminate this data set [Kleinböhl *et al.*, 2009].

[15] In sections 3.1–3.8 we discuss the average and difference temperature fields for the $m = 1$ to $m = 4$ fields. Sections 3.1–3.8 will describe our observations, highlighting the likely dominant waves, wave amplitudes, phases and structure in each field and compare results to expectations on the basis of previous observations and modeling studies.

3.1. T-Average Field $m = 1$

[16] Previous modeling efforts [e.g., Wilson and Hamilton, 1996] predict that the $m = 1$ T-average field

would primarily consist of the $s = 1$ stationary wave with additional minor contributions from $s = 1$ and $s = 3$ semi-diurnal nonmigrating tides. Several previous observational studies have analyzed stationary waves in both hemispheres [Banfield *et al.*, 2000, 2003; Hinson *et al.*, 2003] and the results from this new data set compare well. We find evidence of the $s = 1$ stationary waves in both hemispheres. Wave amplitudes maximize in the middle to high latitudes for this field with a clear seasonal cycle shown at equinoxes and solstices in Figures 5 and 6.

[17] The southern hemisphere stationary wave reaches a maximum of nearly 10 K near $L_s = 90$ at 30–100 Pa altitude at 55–60 S (Figure 5b). A secondary maxima in the vertical is present near 1.5 Pa with an amplitude of 8 K (Figure 5b). Amplitudes fall to near 1 K near southern summer solstice (Figure 5d). Two distinct maxima in the vertical are present from L_s 345–225 during the coldest periods of the year in the southern hemisphere (Figures 5a–5c). The maxima move downward and poleward in location as the winter solstice is approached, and then recede upward and equatorward away from solstice (e.g., at 30–50 Pa and 0.9–1.5 Pa above 45–50 S at $L_s = 0$). There is a prominent westward phase tilt with height associated with the wave. In the lower levels of 50–55 S at $L_s = 90$, the phase (east longitude of maximum amplitude) is 50–65 E within the maxima near 100 Pa (Figure 6a). Vertical wavelength is near 8 scale heights (Mars scale height is 11 km), in excellent agreement with results from MGS TES [Banfield *et al.*, 2003] and RO [Hinson *et al.*, 2003]. Both maxima are directly aligned within the zonal wind jet core [see McCleese *et al.*, 2010, Figures 6 and 7]. Hinson *et al.* [2003] used MGS RO and TES limb observations in conjunction with Mars GCM simulations to analyze the $s = 1$ stationary wave in late southern winter (L_s 150–160) between 65 and 70 S. MCS data do not extend quite as low in the atmosphere as MGS TES and RO, but where there are overlapping (200–1 Pa) data sets, our results compare very favorably in both phase and amplitude.

[18] In the northern hemisphere, there is considerably less identifiable structure to the $m = 1$ stationary wavefield. Additionally we are limited by data in the northern latitudes from $L_s = 255-345$ (e.g., we have no data for areas poleward of 60 N at the northern winter solstice, $L_s = 270$ [see McCleese *et al.*, 2010, Figure 1]. A nearly global dust storm occurred during this time and most profiles were irretrievable. Similar to the southern hemisphere, we observe two maxima in the vertical during equinox (L_s 345–15 and L_s 165–195) with one near 7–11 Pa and the second at 0.9–1.5 Pa altitude above 50–60 N (Figure 5c). Amplitudes associated with these maxima are 3–5 K. For the remainder of northern spring and into northern summer (L_s 15–105), this two maxima structure is absent, before returning as autumn approaches after $L_s = 105$ (Figure 5b). It then persists through the remainder of the year, while moving poleward (i.e., north of 60 N and beyond our available data) as winter approaches. It again appears these maxima follow the core of the jet stream. Note that these two maxima are not the same as those discussed by Banfield *et al.* [2003]. Their upper maxima corresponds to the lower maxima seen in this data. They observed a maxima near the surface at 65 N, but that area is not included in this data for reasons mentioned above. We again find good agreement with MGS TES

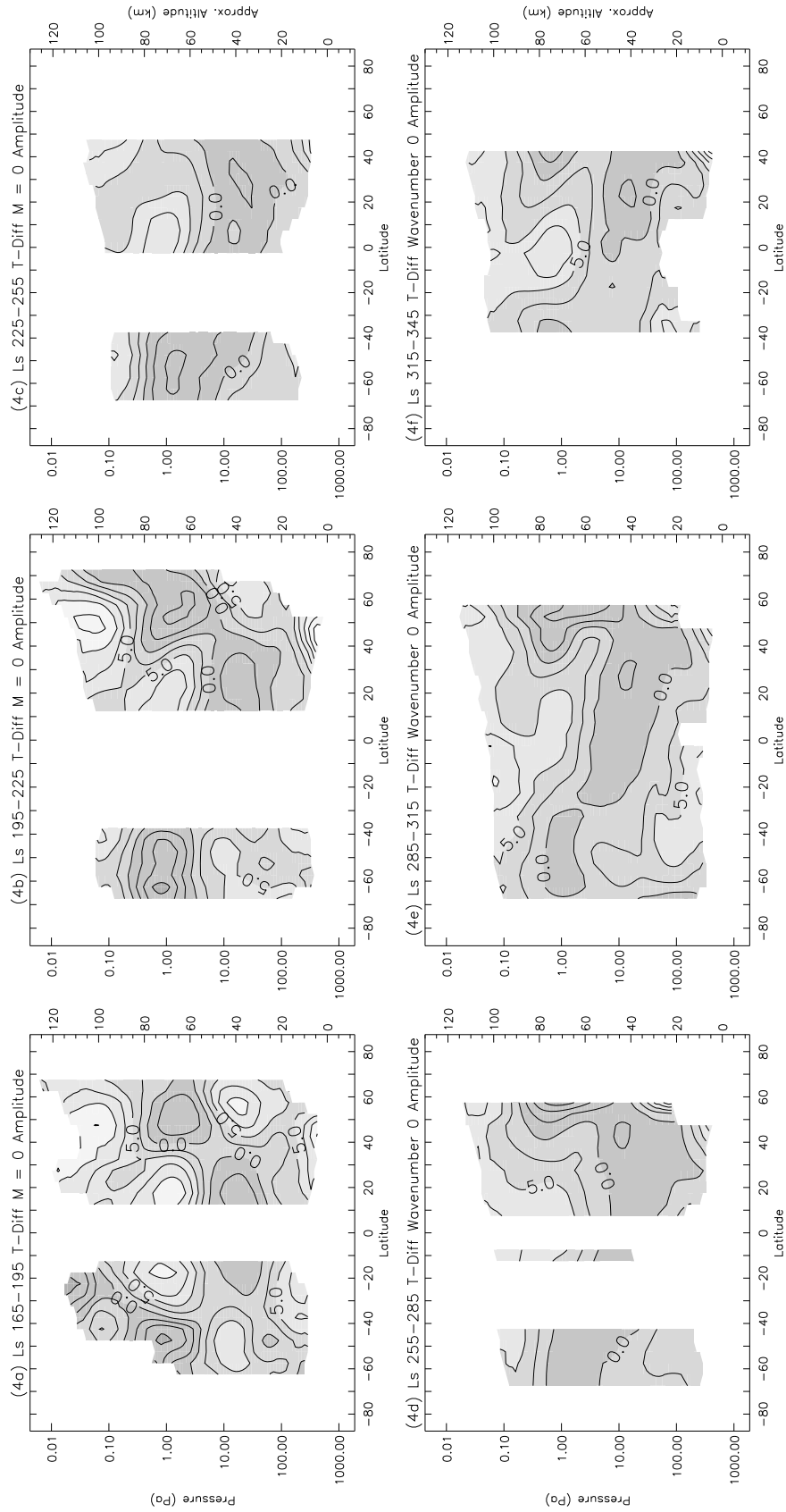


Figure 4. Amplitude of the $m = 0$ T-difference field in Kelvin averaged over 30° of solar longitude for (a) $L_s = 180^\circ$, (b) $L_s = 210^\circ$, (c) $L_s = 240^\circ$, (d) $L_s = 270^\circ$, (e) $L_s = 300^\circ$, and (f) $L_s = 330^\circ$. This field corresponds to the $s = 1$ migrating diurnal tide.

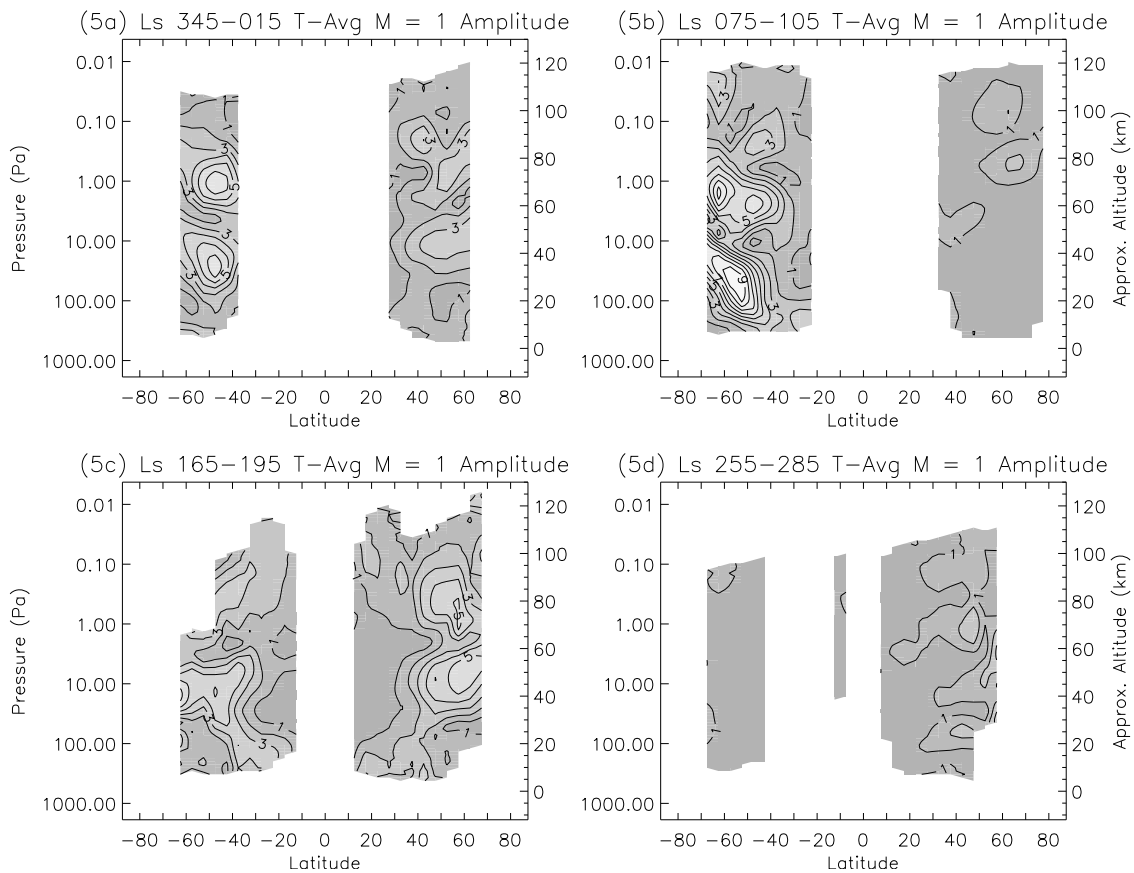


Figure 5. Amplitude of the $m = 1$ T-average field in Kelvins averaged over 30° of solar longitude (a) near northern spring equinox, (b) summer solstice, (c) fall equinox, and (d) winter solstice. This field corresponds to the $s = 1$ stationary wave.

observations with a phase of $35\text{--}40^\circ\text{E}$ at $L_s = 180^\circ$ (Figure 6b) and $\sim 30^\circ\text{E}$ at $L_s = 0^\circ$ (not shown) for the 7–11 Pa maxima above 60°N . On the basis of the amount of phase propagation, the vertical wavelength of the northern hemisphere stationary wave near the equinoxes appears to be function of latitude with it varying from 7.5 to 8 scale heights at 45°N to 9 scale heights at 60°N .

3.2. T-Difference Field $m = 1$

[19] We expect the $m = 1$ T-difference field to primarily consist of the zonally symmetric diurnal tide as well as an $s = 2$ westward diurnal nonmigrating tide. The $s = 1$ topography forces both of these tides, which corresponds to the Tharsis Bulge in the tropics and Hellas Basin in the southern midlatitudes. As discussed below (see Figures 7

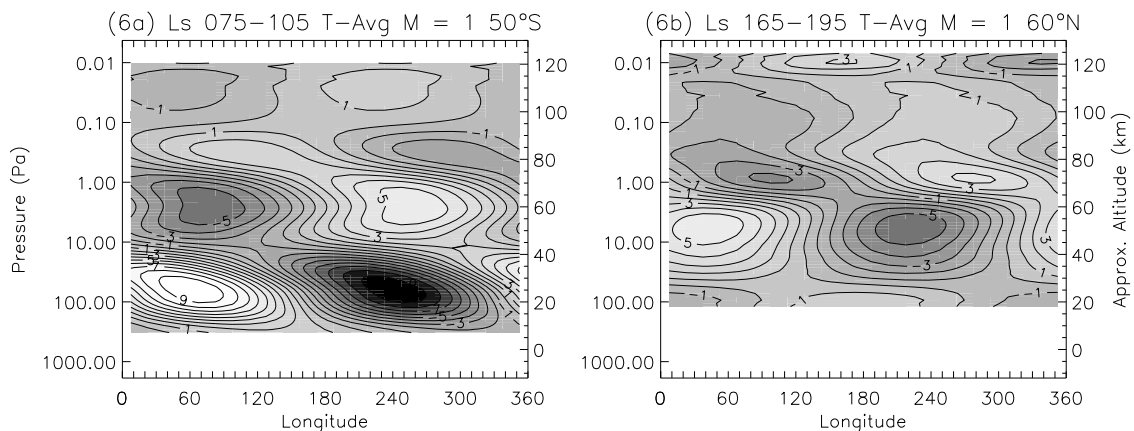


Figure 6. Amplitude and phase of the $m = 1$ T-average field in Kelvins averaged over 30° of solar longitude at (a) 50°S for northern summer solstice and (b) 60°N for fall equinox. Locations of maxima correspond to wave phase at a particular height level.

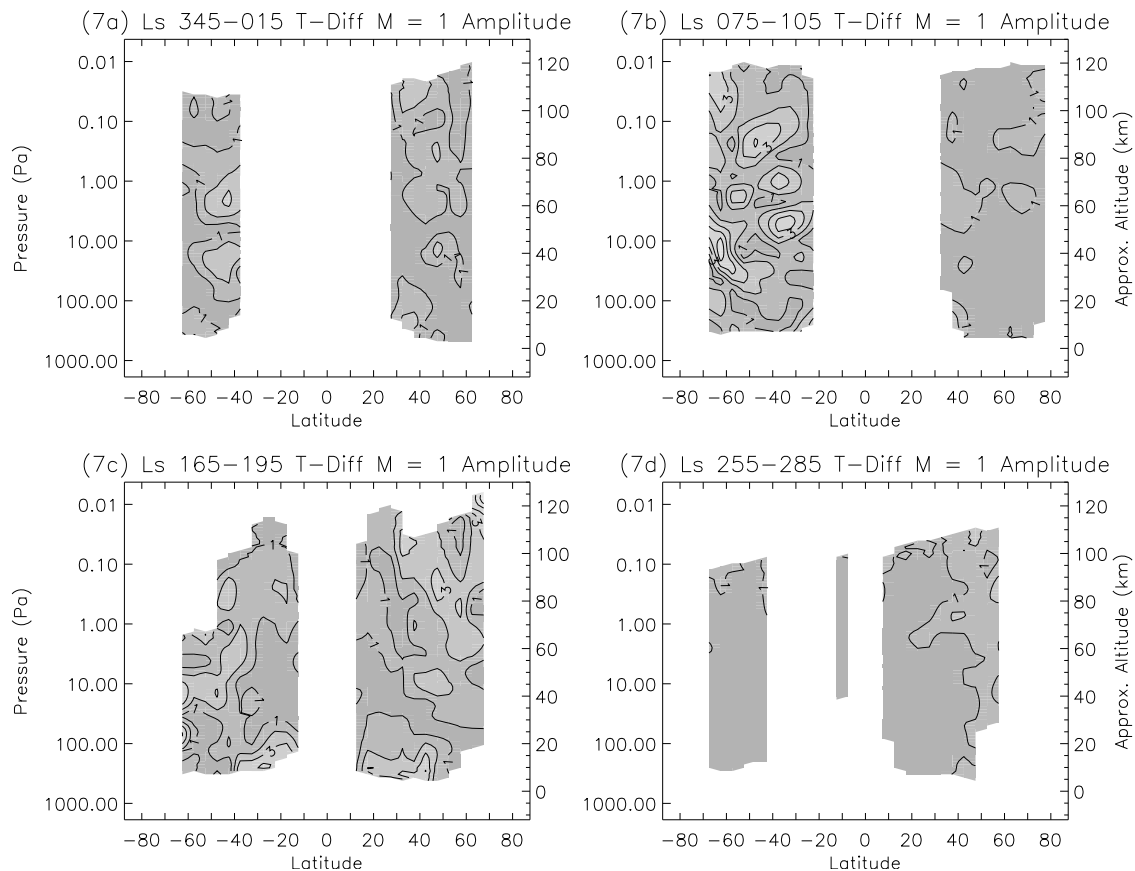


Figure 7. Same as Figure 5 but for the $m = 1$ T-difference field. This field corresponds to the zonally symmetric diurnal tide.

and 8), we find evidence of the zonally symmetric tide in both the tropics and midlatitudes, with notable differences to previous studies, possibly suggesting the presence of the $s = 2$ diurnal tide or interannual variability of the zonally symmetric tide.

[20] The magnitudes of the $m = 1$ T-difference field follow a clear seasonal cycle and this is shown at equinoxes and solstices in Figures 7 and 8. Near equinox ($L_s = 0^\circ, 180^\circ$), the wave amplitudes are generally equatorially symmetric with two 1–3 K maxima in the vertical above $40\text{--}50^\circ$ latitude (Figures 7a and 7c). The first maxima is at 11–30 Pa with the second broadly dispersed above 1.5 Pa (Figures 7a and 7c). Although equatorial data are lacking at $L_s = 0^\circ$, at $L_s = 180^\circ$ there is also an additional maxima in each hemisphere near the surface from 20 to 40° latitude of 3–4 K amplitude. In the solstitial seasons, the summer hemisphere has very weak amplitudes (~ 1 K) with no clear structure while the southern winter hemisphere has amplitudes up to 5 K (Figures 7b and 7d). As mentioned in section 3.1, there are no data for northern winter solstice at high latitudes. The structure of these amplitude maxima are complex during southern winter, with 3–5 distinct maxima in the vertical between 0.3 and 30 Pa altitude above $35\text{--}65^\circ\text{S}$ (Figure 7b). This large amplitude near southern winter solstice is at odds with MGS TES observations [Banfield *et al.*, 2003] which showed only 1–2 K amplitudes during this season. The area of 5 K amplitude 11–30 Pa altitude above 65°S is within the volume of atmosphere sampled by TES nadir observations.

This suggests interannual variability in the zonally symmetric diurnal tide and/or contributions from the $s = 2$ diurnal tide. Banfield *et al.* [2001] noticed variability and enhancement in the zonally symmetric diurnal tide associated with the 2001 global dust storm, but dust opacity levels were approximately one order of magnitude lower during the MCS observations [see McCleese *et al.*, 2010, Figures 10 and 11].

[21] The phase of the maximum of this tide also exhibits a complex pattern that was not observed by TES near southern winter solstice. At $60\text{--}65^\circ\text{S}$, the phase of the maximum is near 220°E near the surface and this is essentially constant up to $50\text{--}83$ Pa altitude. Above that, the phase of the maximum “jumps” to $55\text{--}60^\circ\text{E}$ at $7\text{--}30$ Pa (Figure 8a). This longitude corresponds to the western rim of Hellas Basin. Above this the phase then progresses steadily eastward to return to near 220°E at the top of the observable column (Figure 8a). At latitudes equatorward of the maxima (i.e., $40\text{--}55^\circ\text{S}$), the phase propagates significantly in low levels, with a steep westward tilt, and does not exhibit the “jump” in phase seen farther south (Figure 8b). The phase is westward tilted below 7 Pa and then tilted eastward above that until 0.2 Pa (Figure 8b). This phase behavior is seen from $L_s = 75\text{--}135^\circ$ during the coldest part of the year, with clearly delineated westward phase tilt with height for nearly the entire column at southern middle and high latitudes immediately before and after this time. This large westward phase propagation in the lowermost levels is suggestive of a surface-

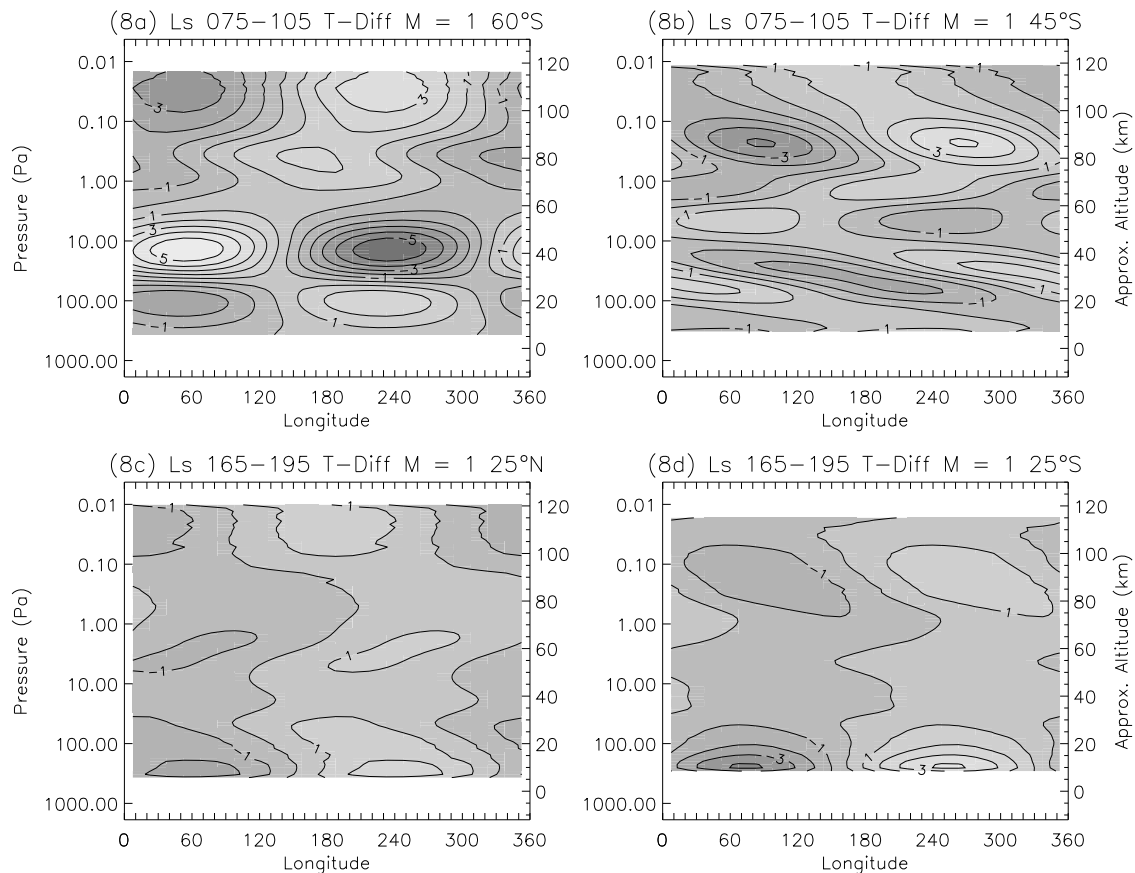


Figure 8. Amplitude and phase of the $m = 1$ T-difference field in Kelvins averaged over 30° of solar longitude at for northern summer solstice for (a) 60°S and (b) 45°S . The same field for fall equinox at (c) 25°S and (d) 25°N shows a very similar pattern spanning the tropics indicative of the zonally symmetric diurnal tide. Locations of maxima correspond to wave phase at a particular height level.

forced $s = 2$ westward diurnal nonmigrating tide. Tidal theory suggests the gravest Hough mode contributing to this tide has a wavelength of ~ 32 km, which is roughly consistent with the ~ 40 – 45 km wavelength implied by the rate of phase propagation seen in Figure 8b.

[22] The phase associated with the near surface tropical maxima of 2–4 K near the northern fall equinox (L_s 135–195°), is clearly in phase with the high terrain of Tharsis at 240–270°E and nearly barotropic with height (Figures 8c and 8d). The zonally symmetric diurnal tide can be thought of as a daily pulsing of the atmosphere and is expected to be in phase with the heating of high terrain, and this result is consistent with that. It is not clear which Hough mode is present in the wavefield to contribute to the zonally symmetric diurnal tide and was thus not plotted in Figure 2.

3.3. T-Average Field $m = 2$

[23] We expect the $s = 2$ stationary wave to dominate the $m = 2$ T-average field with additional minor contributions from the semidiurnal zonally symmetric tide and the $s = 4$ semidiurnal nonmigrating tide. We observe the $s = 2$ stationary wave in both hemispheres and find features generally consistent with previous studies. Similarly to the $s = 1$ stationary wave, the $s = 2$ stationary wave temperature maxima align with the jet streams [McCleese *et al.*, 2010]. Relevant plots to this field are in Figures 9 and 10 which shows the

equinoctial periods and time periods prior to each solstice, when the $s = 2$ stationary wave reaches its maximum amplitude in the hemisphere approaching winter solstice.

[24] Previous studies have shown [e.g., Hollingsworth and Barnes, 1996] that the $s = 2$ and $s = 1$ stationary waves have comparable amplitudes in the northern hemisphere, but that the southern hemisphere is dominated by the $s = 1$ wave. The $s = 2$ and $s = 1$ dominated topography in the northern and southern hemisphere high latitudes, respectively, is the driving force for this difference. Banfield *et al.* [2003] generally confirmed this, with a clear $s = 1$ stationary wave preference in the southern hemisphere and an $s = 2$ preference in northern hemisphere low levels and $s = 1$ at higher levels. MCS observations show that the $s = 2$ stationary wave is stronger than the $s = 1$ wave in the northern hemisphere at nearly all observed times of year and altitudes, with the sole exception near $L_s = 180^\circ$ (compare Figures 5 and 9). The southern hemisphere stationary waves in the low levels consistently align themselves with the polar jet, tilting upward and poleward from the surface near 45°S (Figures 5b and 9b).

[25] Within the limits of our data availability (see section 3.1), we see a similar structure to that observed by Banfield *et al.* [2003] for the $s = 2$ stationary wave in both hemispheres at lower altitudes. The maximum wave amplitude (5 K) in the southern hemisphere occurs before

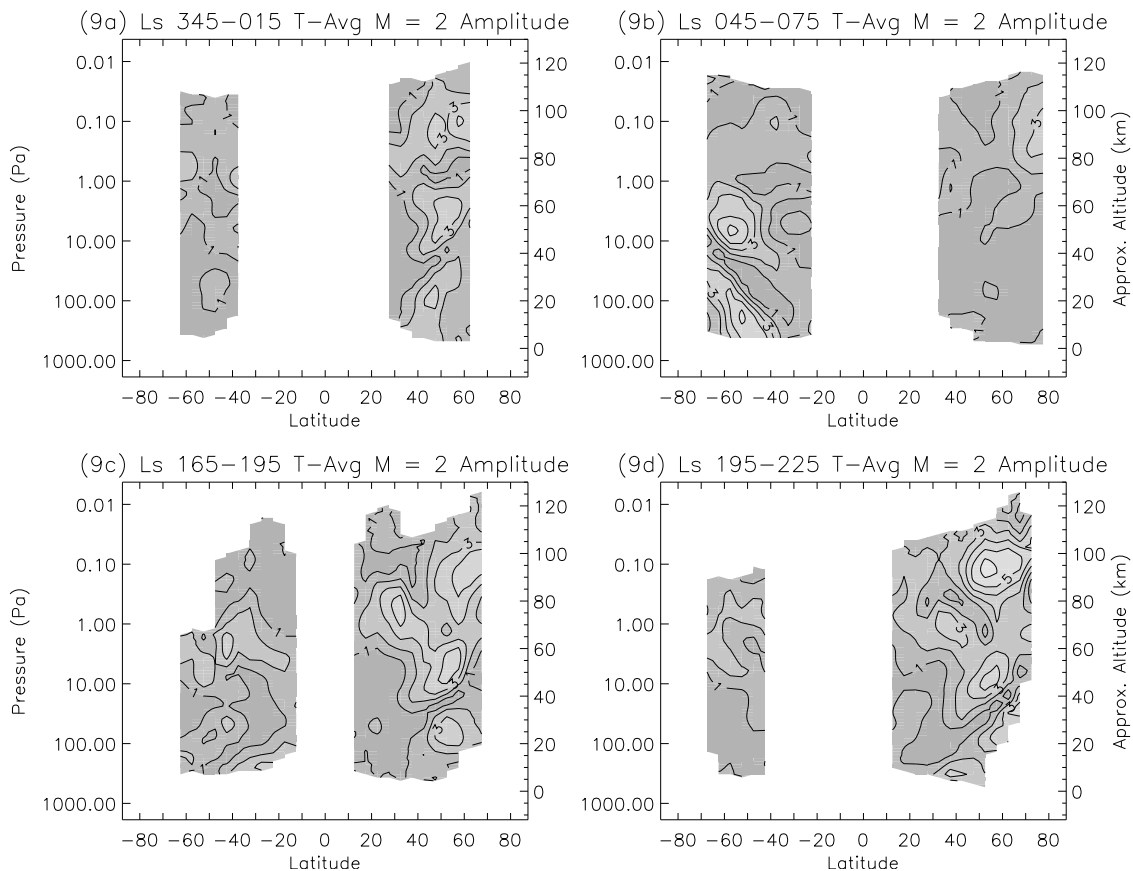


Figure 9. Amplitude of the $m = 2$ T-average field in Kelvins averaged over (a) 30° of solar longitude near northern spring equinox, (b) late northern spring near $L_s = 60^\circ$, (c) fall equinox, and (d) northern fall near $L_s = 210^\circ$. This field corresponds to the $s = 2$ stationary wave.

southern winter solstice at $L_s = 45\text{--}75^\circ$, with two distinct maxima in the vertical (Figure 9b). The lowermost maximum is at 200–300 Pa above 50°S and the upper at 70–90 Pa above 55°S (Figure 9b). Each maxima has a distinct phase shift, with a phase of the maximum near 45°E for the lower maxima and 135°E for the upper maxima (Figure 10a). *Banfield et al.* [2003] found the same phases and associated this 90° phase shift with an evanescent wave beyond the polar jet duct on the basis of a region of negative quasi-geostrophic index of refraction. However, the coherent phase propagation with height and large amplitude associated with the higher maxima argue against evanescence and suggest a vertically propagating wave. *Hinson et al.* [2003] showed that using quasi-geostrophic theory near the Martian winter polar jets should be done with “caution,” and this possibly led to a spurious result in predicting wave evanescence in this region. As with the $s = 1$ stationary wave, our analysis of the $s = 2$ southern stationary wave compares very favorably with *Hinson et al.* [2003] in amplitude and phase.

[26] The pattern in the northern hemisphere lower atmosphere is similar to that in the southern hemisphere and that seen by MGS TES with an approximately barotropic structure in the lowermost few scale heights of the atmosphere and a phase near $40\text{--}45^\circ\text{E}$ (Figures 10b and 10c). However, the structure and amplitude in the middle atmosphere of the northern hemisphere is significantly different from that of the southern hemisphere. A 3–5 K maximum is present year

round near 0.2–0.08 Pa altitude and moves through the middle and high latitudes, depending on season (Figure 9). In colder times of the year, the maxima is shifted equatorward to near 50°N , while in the warmer seasons, it moves to very high latitudes ($>75^\circ\text{N}$; see Figure 9). The phase of this amplitude maximum also follows a seasonal cycle, with a minimum near 60°E near summer solstice and a maximum at 120°E just before winter solstice (Figures 10b and 10c). The change in phase of the maximum and movement of the amplitude maxima through the Martian year is consistent with the movement of the polar jet with season.

3.4. T-Difference Field $m = 2$

[27] The eastward propagating diurnal Kelvin wave 1 (DK1) has been shown previously to dominate the $m = 2$ T-difference field with additional contributions from the westward propagating diurnal $s = 3$ nonmigrating tide. Both of these tides are forced by the interaction of the diurnal migrating tide with the $s = 2$ topography. DK1 has been observed or inferred in numerous previous data sets including Mariner 9 [*Conrath*, 1976], Viking landers [*Leovy*, 1981], MGS aerobraking [*Forbes and Hagan*, 2000; *Wilson*, 2002], MGS RO [*Hinson et al.*, 2001], and MGS TES [*Wilson*, 2000; *Banfield et al.*, 2000, 2003]. It has been extensively studied using Mars GCMs [*Wilson and Hamilton*, 1996; *Bridger and Murphy*, 1998; *Lewis and Barker*, 2005]. This is the first observation of DK1 in the

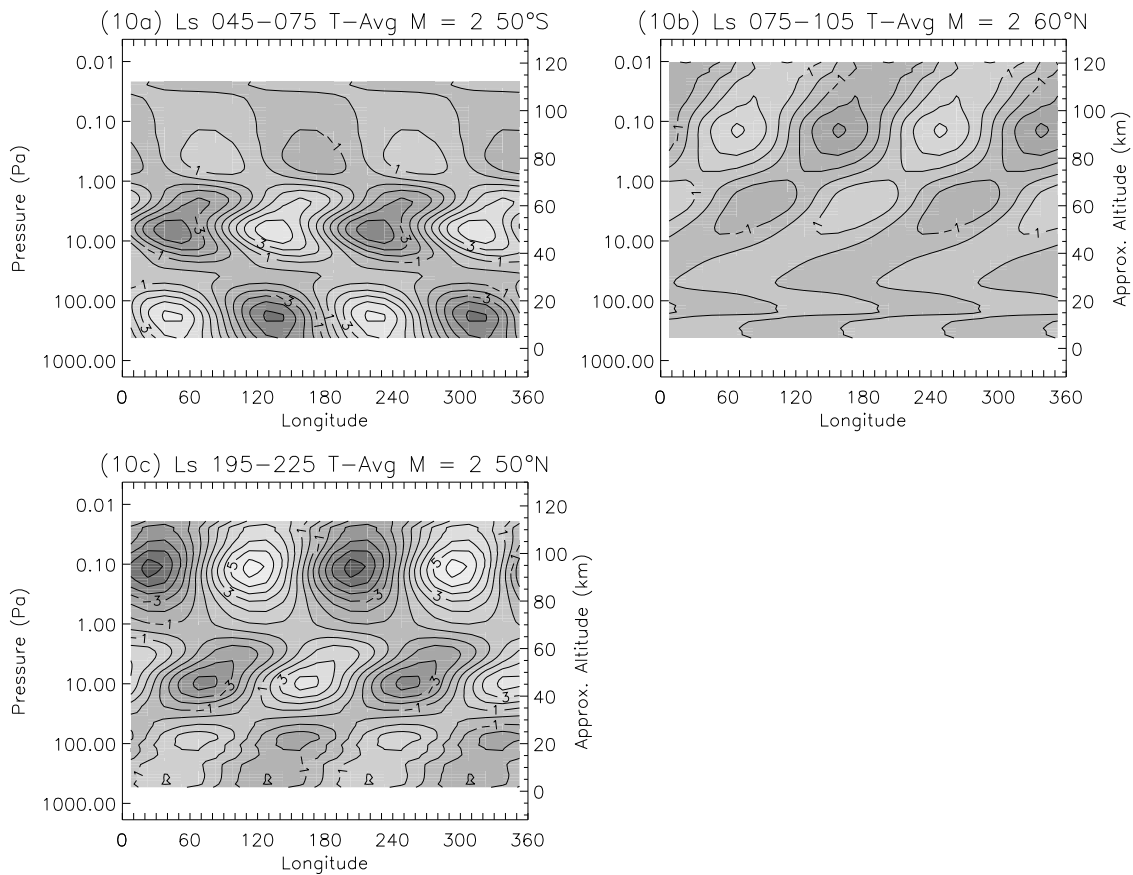


Figure 10. Amplitude and phase of the $m = 2$ T-average field in Kelvins averaged over (a) 30° of solar longitude at $L_s = 60^\circ$ for 50°S , (b) northern summer solstice at 60°N , and (c) $L_s = 210^\circ$ for 50°N . Locations of maxima correspond to wave phase at a particular height level. Notice the phase shift for the northern hemisphere maxima near 0.1 Pa between the two seasons.

middle atmosphere. *Hinson and Wilson* [2004] compared MGS RO data with Mars GCM output and found the westward diurnal wave 3 tide has an amplitude of ~ 2 K and a vertical wavelength of ~ 20 km in the tropics. Not unexpectedly, we find the amplitude, structure and phase of DK1 to be consistent with previous studies in most respects.

Figures 11 and 12 show amplitude and phase, respectively, averaged over 90° of L_s and show one period surrounding equinox and one surrounding solstice which both include tropical data.

[28] The work mentioned above typically found amplitudes of 1–3 K for DK1, and our results are generally

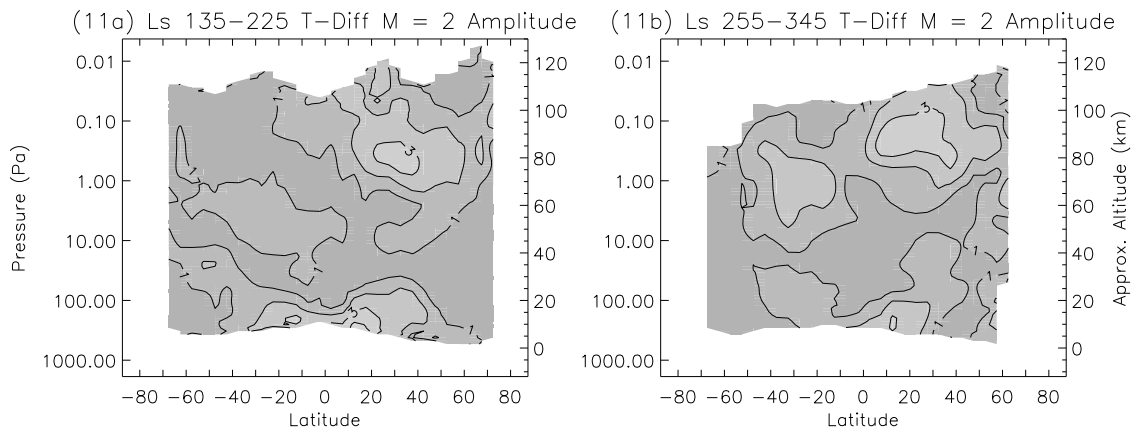


Figure 11. Amplitude of the $m = 2$ T-difference field in Kelvins averaged over (a) 90° of solar longitude surrounding northern fall equinox and (b) 90° of solar longitude corresponding to late northern fall through most of winter. This field corresponds to DK1.

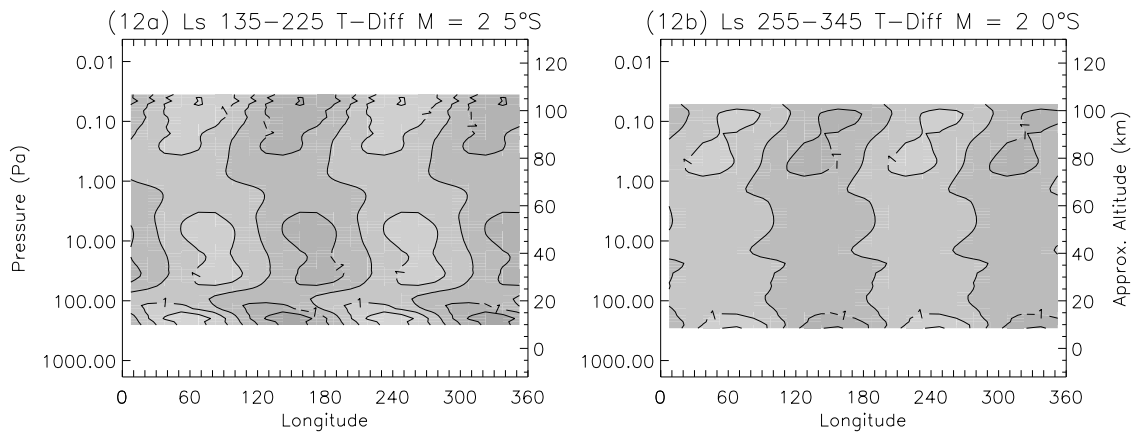


Figure 12. Amplitude and phase of the $m = 2$ T-difference field in Kelvins averaged over (a) 90 of solar longitude surrounding northern fall equinox and (b) 90 of solar longitude corresponding to late northern fall through most of winter. Notice the lack of significant phase shift through the profile, diagnostic of DK1.

consistent with this, however we do find amplitudes in this field up to 5 K (not shown) at particular locations and seasons (e.g., $L_s = 180$ above 30 N). This could be due to contributions from the $s = 3$, $\sigma = 1$ tide and higher tidal harmonics or seasonal variability of DK1. We find the northern hemisphere favored in the amplitudes of this field, with a persistent (nearly year-round) meridionally broad 2–3 K maxima between 10 and 40 N near 0.2–0.6 Pa (Figure 11). A similar middle atmosphere maxima is seen in the southern hemisphere at similar latitudes, but lower in the atmosphere (2.5–6.8 Pa) and weaker in magnitude (1–2 K; see Figure 11). Low-altitude amplitudes also favor the northern hemisphere. Broad 1–3 K amplitudes exist between 40 S and 40 N during most of the year (by extrapolation for times of year where equatorial data are missing), but typically peak between 10 and 20 N. Areas within 20 S–20 N between 1 and 100 Pa seem devoid of significant amplitude (>1 K) at all times of year (Figure 11). That result is persistent when averaging over 90 of solar longitude. That altitude range is where dust concentrations maximize in nearly all seasons [McCleese *et al.*, 2010] and is near the altitude of the “High Altitude Tropical Dust Maximum” observed by Heavens *et al.* [2011b]. It has been suggested that the presence of airborne dust can push the Kelvin wave away from resonance, but despite this, its amplitude should remain relatively invariant [Wilson and Hamilton, 1996; Leovy and Zurek, 1979].

[29] We find a phase of the maximum near 60 E associated with DK1, consistent with the expectation of 15 of eastward propagation between the 14:00 observations of MGS TES (which found the phase near 45 E) and the 15:00 observations of MCS. The phase is essentially constant with height, a diagnostic feature of DK1 (Figure 12). It also becomes clear from analysis of the phase that the middle atmosphere maximum in the southern hemisphere is not associated with DK1, while the northern hemisphere maximum clearly is. In the southern hemisphere maximum, there is significant (typically $>70^\circ$) eastward phase propagation over the observable domain, which suggests that this maximum is not associated with the westward propagating $s = 3$, $\sigma = 1$ tide (not shown). There is a similar area of eastward

phase propagation typically at a lower altitude in the northern hemisphere below the maximum associated with DK1 (not shown). However, this region has low amplitudes (<1 K or less) at all times of year. The near-surface maxima observed in most seasons is also clearly associated with DK1.

[30] Additionally, we analyzed the 15:00 and 03:00 LST $m = 2$ fields individually and calculated phase profiles. These fields thus include contributions from waves that appear in both the $m = 2$ average and difference fields. Despite this, there is still a clear signature of DK1 in the tropics with a 180 phase shift between the morning and afternoon profiles (indicative of a diurnal wave) and a roughly barotropic profile with height.

[31] While the gravest eastward propagating wave number 1 diurnal Hough mode (DK1 in Figure 2) is equatorially symmetric, Forbes and Hagan [2000] found in their model that this mode would be distorted and coupled into an asymmetric mode through interaction with the highly asymmetric zonal mean wind field during solstitial periods (see McCleese *et al.* [2010, Figures 6 and 7] for MCS-derived zonal mean winds). This first asymmetric mode possesses a vertical wavelength of ~ 61 km on Mars. As can be seen in Figure 13, the $m = 2$ T-difference field does possess both symmetric and antisymmetric components with amplitudes of 1–2 K (compare with Figures 11a and 11b). The phase of the symmetric field matches expectations of the Kelvin mode with a nearly barotropic phase profile. The antisymmetric phase profile shows steady eastward propagation, particularly during the winter solstitial period, when the zonal mean winds are strongly asymmetric and this mode should be more strongly excited. The amount of phase progression through the column indicates a vertical wavelength of ~ 65 –70 km (Figure 14), very close to the theoretical wavelength.

3.5. T-Average Field $m = 3$

[32] We expect that the $s = 3$ stationary waves and two nonmigrating tides ($s = 1$, $\sigma = 2$ and $s = 5$, $\sigma = 2$) will primarily contribute to the $m = 3$ T-average field. Banfield *et al.* [2003] found generally weak amplitudes with disorganized structures in this field in the lower atmosphere, and

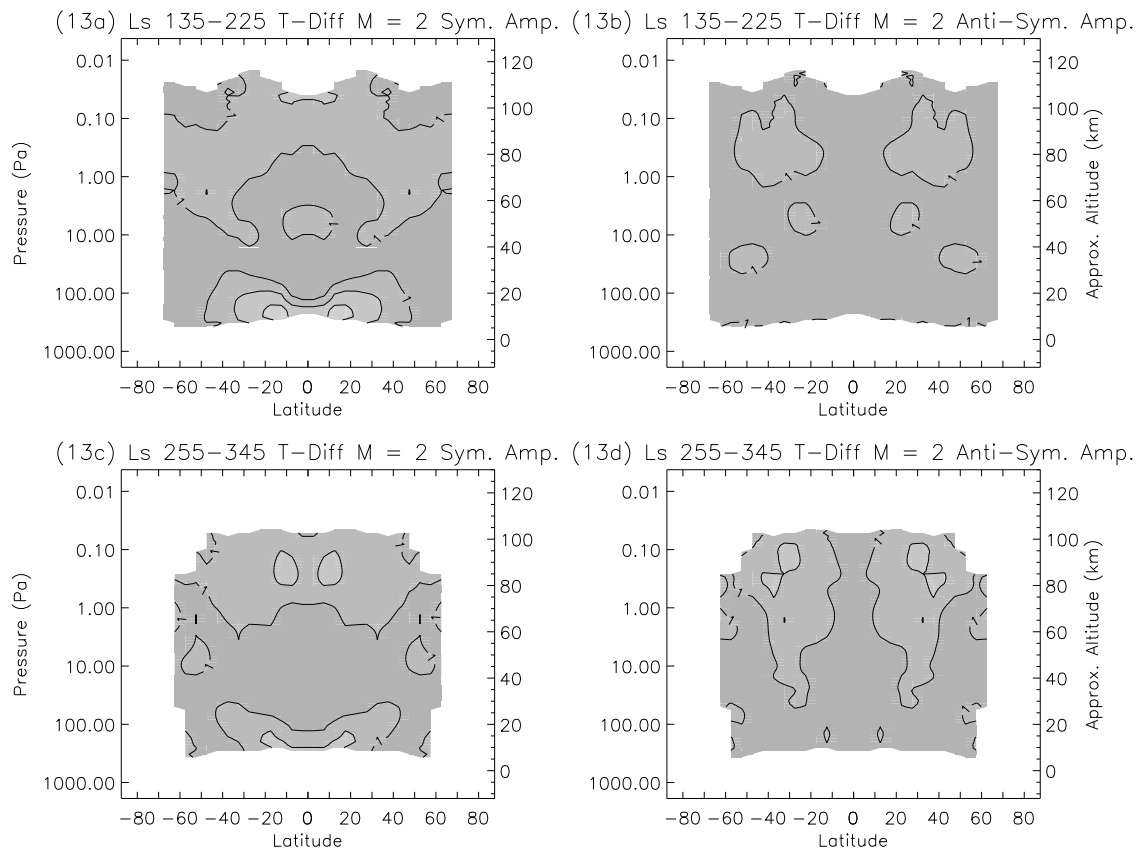


Figure 13. Amplitude of the (a and c) symmetric and (b and d) antisymmetric components of the $m = 2$ T-difference field in Kelvins averaged over 90° of solar longitude surrounding northern fall equinox (Figures 12a and 12c) and 90° of solar longitude corresponding to late northern fall through most of winter (Figures 12b and 12d). This field corresponds to DK1.

we confirm that result with some differences in specifics. Below we describe evidence of the $s = -1$, $\sigma = 2$ tide (possibly the semidiurnal Kelvin $s = 1$ wave) in the northern hemisphere midlatitude middle atmosphere and compare its observed features to previous studies. Figure 15 shows the amplitude and phase of this field at $L_s = 90^\circ$ when the $s = -1$, $\sigma = 2$ tide is most readily identifiable. We find no persuasive evidence of the $s = 3$ stationary waves in either hemisphere.

[33] Using MGS TES data, *Banfield et al.* [2003] observed the maximum for this field of order 2–4 K in the lowest scale height of the low latitudes and generally less than 1 K elsewhere in its observable domain. MCS observations in the lowest scale height of the tropical atmosphere are sparse, so we cannot confidently exclude the existence of a similar maximum in this data. At best we see ~ 1 K amplitude near 45°S (Figure 15a), which is a latitude that MGS TES observed a persistent maximum [*Banfield et al.*, 2003]. From $L_s = 135\text{--}195^\circ$ where tropical data are available, we do see a broad area of 1–2 K amplitudes between 35°S and 35°N with up to 3 K near fall equinox (not shown). This maximum does not appear later in the year (near $L_s = 300^\circ$) when tropical data are again present.

[34] In the middle atmosphere, however, we see a persistent 1–3 K maximum in each hemisphere above the middle and high latitudes. *Barnes et al.* [1996], *Hollingsworth and Barnes* [1996], and *Banfield et al.* [2003] all noted that the

$s = 3$ stationary wave is not expected to propagate significantly vertically. In the northern hemisphere, a maximum of 2–3 K is present year round (within data limitations, there are no data for $L_s = 330^\circ$ at those latitudes) at 0.01–0.6 Pa altitude above $40\text{--}60^\circ\text{N}$ (Figure 15a). This maximum has a steady phase of $70\text{--}85^\circ\text{E}$ year round, with variability within that bound (Figure 15b). It also exhibits an eastward tilt with height. We identify this as the $s = -1$ eastward propagating semidiurnal tide, probably the semidiurnal Kelvin wave (SK1). The gravest Hough mode contributing to SK1 is meridionally broad, so it is expected to have appreciable amplitude at high latitudes (Figure 2). On the basis of $\sim 60\text{--}90^\circ$ of phase change within the deep layer of the middle atmosphere with an eastward tilt, it appears this tide has a long vertical wavelength, but we cannot get a confident value since it is near the top of the MCS domain. SK1 is evanescent with a vertical wavelength of 14 scale heights, so this appears roughly consistent [*Withers et al.*, 2003]. *Wilson* [2002] observed this tide at thermospheric altitudes. We cannot confidently identify this tide in the southern hemisphere, where the $m = 3$ T-average field is poorly organized and less structured than the northern hemisphere. At best there are suggestions of this tide in the southern hemisphere near $L_s = 150^\circ$, when the high-altitude pattern is roughly equatorially symmetric and there is a broad 2 K maximum over the southern middle and high latitudes at comparable heights to that in the north and a weak eastward phase tilt

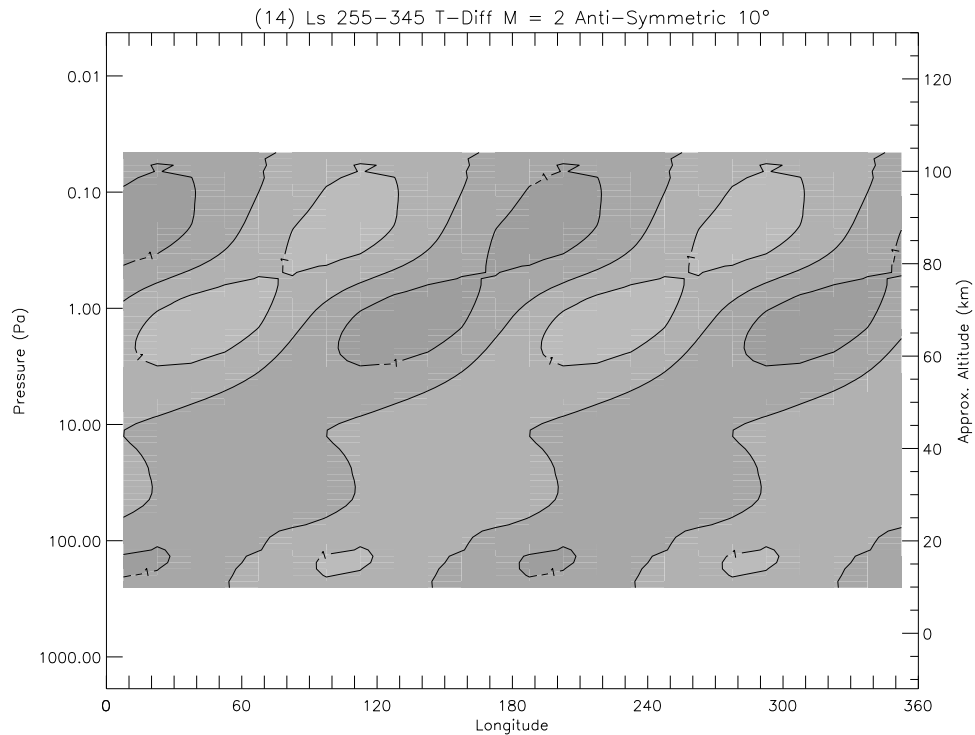


Figure 14. Amplitude and phase of the antisymmetric component of the $m = 2$ T-difference field in Kelvins at 10° latitude averaged over 90° of solar longitude corresponding to late northern fall through most of winter.

with height (not shown). Lower-altitude maxima that appear early in the year are not associated with this tide and exhibit no structured phase pattern. General circulation modeling is required to further illuminate the expected amplitudes and phase propagation of this tide and corroborate this identification.

3.6. T-Difference Field $m = 3$

[35] The $s = 2$ diurnal Kelvin wave (DK2) is expected to dominate the $m = 3$ T-difference field, with additional contributions from the $s = 4$, $\sigma = 1$ nonmigrating tide. These two tides likely result from the interaction of the diurnal

migrating tide with the $s = 3$ component of the topography. DK2 has been detected previously in many of the studies that detected DK1 [e.g., *Wilson, 2000*]. Classical tidal theory suggests a 90–100 km vertical wavelength and 1–2 K amplitude [*Wilson and Hamilton, 1996; Longuet-Higgins, 1968; Forbes et al., 2002*; R. J. Wilson, personal communication, 2 June 2011]. *Hinson and Wilson [2004]* compared MGS RO data with Mars GCM output and found the westward diurnal wave 4 tide has an amplitude of ~ 2 K and a vertical wavelength of ~ 20 km in the tropics. We find DK2 to have an amplitude and phase consistent with previous studies, but the deeper profile that MCS provides indicates

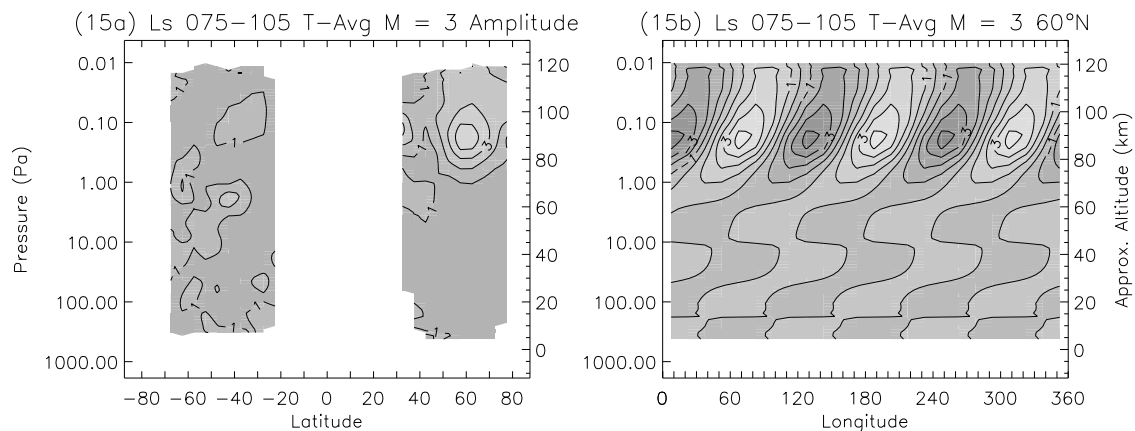


Figure 15. (a) Amplitude of the $m = 3$ T-average field in Kelvins averaged over 30° of solar longitude surrounding northern summer solstice and (b) amplitude and phase of the same field at 60°N highlighting SK1. This field corresponds to the $s = 3$ stationary wave and SK1.

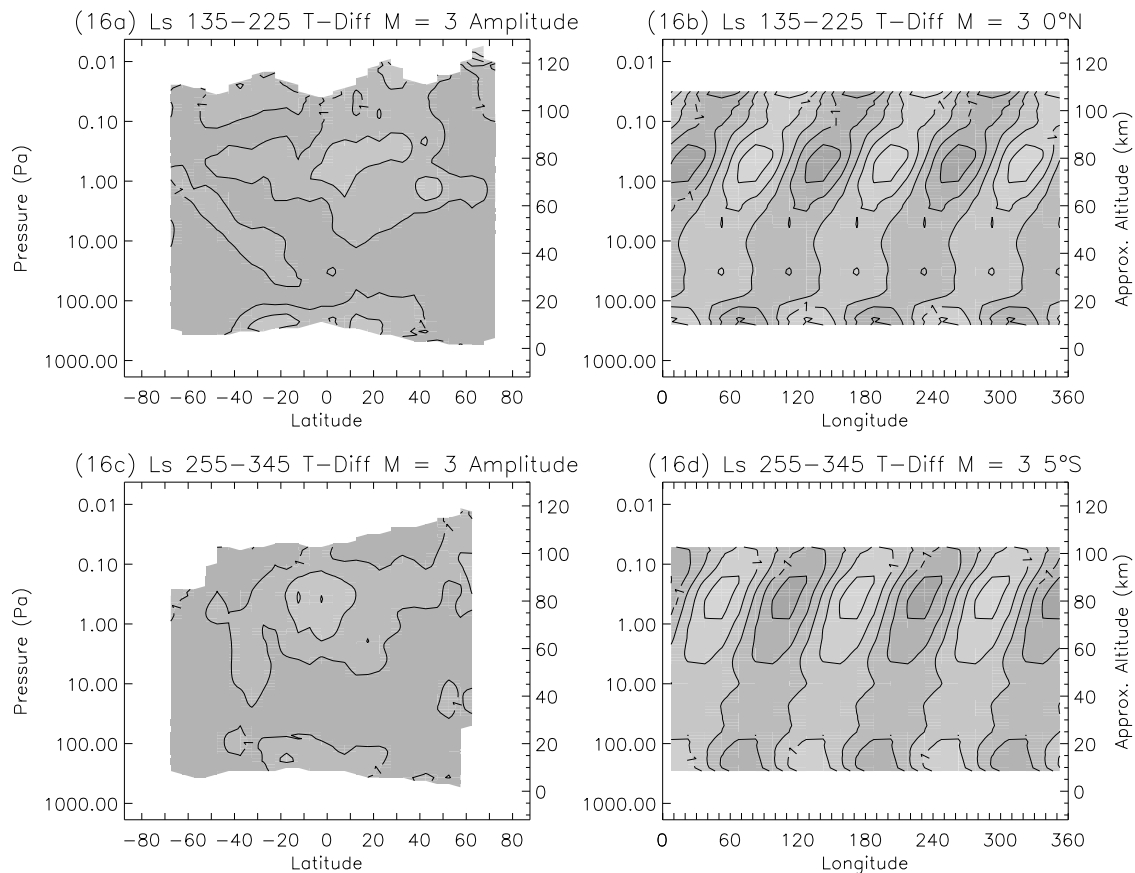


Figure 16. (a) Amplitude of the $m = 3$ T-difference field in Kelvins averaged over 90° of solar longitude surrounding northern fall equinox and (b) amplitude and phase of the same field at 0°N . Also shown are (c) the same field averaged over 90° of solar longitude corresponding to late northern fall through most of winter and (d) amplitude and phase of the same field at 5°S . These plots highlight DK2.

its vertical wavelength is longer than what classical tidal theory suggests. See Figure 16 (which covers the same two 90° of L_s time periods as shown for DK1) and the discussion below.

[36] Given that DK2 is expected to be relatively consistent seasonally in its traits, we use data averaged over 90° of solar longitude to diminish the possible effects of seasonal variability in other aliased tides. We find a broadly equatorially symmetric pattern in this field's amplitudes, with most amplitude concentrated in the tropics. The exception is near the equinoxes, when larger amplitudes also exist in the middle atmosphere above the midlatitudes. Much like DK1, we see a near surface maximum in the tropics and then a large area of weak amplitude from ~ 5 –100 Pa. Then another area of 1–2 K amplitude exists above that level with generally increasing amplitudes with height (Figures 16a and 16c). Near the top of the MCS domain, the amplitudes decrease again. Since it is known that both DK1 and DK2 propagate well beyond the MCS vertical domain to aerobraking altitudes and have significant amplitudes there, we expect this apparent maximum between 0.1 and 1 Pa to be a local maximum.

[37] We find values of DK2's phase of the maximum to be near 15°E in the lowest altitudes for a 15:00/03:00 LST orbit, consistent with MGS TES observed values of 0°E at 14:00/02:00 LST [Banfield et al., 2003] (Figures 16b and

16d). This is consistent throughout the year (when near-equatorial data are available) and meridionally within a particular season to $\sim 30^\circ$ latitude. The amount of eastward phase progression with height is also consistent with modeling [see Wilson, 2000, Figure 5b] and is typically $\sim 80^\circ$ from the surface to 0.1 Pa (≈ 8.5 scale heights). This argues that the vertical wavelength of DK2 is ≈ 140 km, longer than tidal theory suggests.

[38] As with the $m = 2$ T-difference field, we decomposed this field into symmetric and antisymmetric components. There was little or no amplitude associated with the antisymmetric field and the phase profiles did not indicate a coherent propagating wave (not shown). This result implies that the symmetric Kelvin mode is dominating this field.

[39] The temperature maxima found in this field near equinox in the midlatitudes (poleward of 40°) of both hemispheres at 1 Pa is not associated with DK2. These maxima are markedly equatorially symmetric and display similar phase behavior with a westward tilt with height below the altitude of the maxima (not shown). It is unclear, at present, which wave is responsible for this behavior, but it is worthy of further investigation through general circulation modeling, given their 3–5 K amplitude near northern spring equinox and ~ 3 K at fall equinox.

[40] Withers and Catling [2010] compared MCS data with the Phoenix entry temperature profile and identified

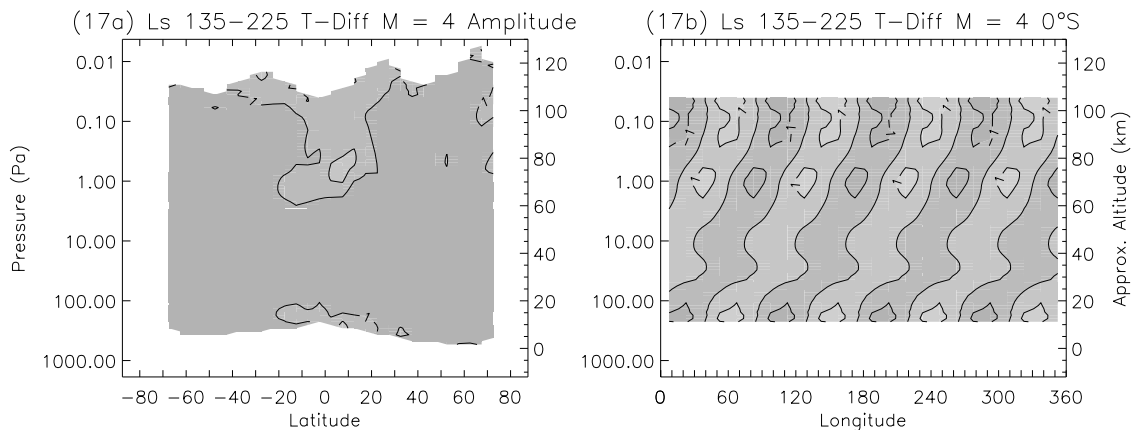


Figure 17. (a) Amplitude of the $m = 4$ T-difference field in Kelvins averaged over 90° of solar longitude surrounding northern fall equinox and (b) amplitude and phase of the same field at 0° S. These plots highlight DK3.

temperature variations owing to either DK2 or the SK1. They also noticed 60° of eastward phase propagation between 3 Pa and 0.03 Pa. We see $50\text{--}60^\circ$ of eastward phase change in both the $m = 3$ average and difference fields with our 30° of solar longitude average, consistent with their value given they only used 6° of solar longitude averaging (not shown). SK1 would be found in the average field, and as mentioned in section 3.5, we see evidence of its presence at this location ($40\text{--}60^\circ$ N) year round. Although DK2 is not as meridionally broad as DK1, theory still implies some presence at these latitudes and it appears present in MCS data, particularly at higher altitudes. As with DK1, we analyzed the morning and afternoon fields individually to determine the phase change over half a sol and find that the primary pattern is neither diurnal nor semidiurnal at these latitudes and altitudes, with $50\text{--}120^\circ$ of phase shift above the lowest few scale heights (not shown). For a solely semidiurnal pattern, 360° of phase shift is expected (making it appear to have no phase shift) while 180° is expected for a solely diurnal pattern. Amplitudes are ~ 3 K for both the $m = 3$ average and difference fields at high altitudes above $65\text{--}70^\circ$ N around $L_s = 75^\circ$ (using both $L_s = 60^\circ$ and 90°), suggesting that both SK1 and DK2 were contributing approximately equally to the profile observed by Phoenix upon Mars atmospheric entry.

3.7. T-Average Field $m = 4$

[41] The $s = 4$ stationary waves and an eastward propagating $s = 2$ semidiurnal tide (including semidiurnal Kelvin wave 2, SK2) contribute to the $m = 4$ T-average field, in addition to an $s = 6$, $\sigma = 2$ tide. As other studies have mentioned [e.g., Hollingsworth and Barnes, 1996], $s = 3$ and higher stationary waves are not expected to propagate significantly vertically, so amplitudes in the middle atmosphere should be from tides. Tidal theory and the limited observations of SK2 identify it as a vertically evanescent “edge” wave with roughly constant phase vertically and meridionally. It also should have a low-temperature amplitude, about 0.5 K according to GCM simulations [Hinson et al., 2008]. Despite that, SK2 is near resonance in the Martian atmosphere and creates large variations in surface pressure [Zurek, 1988; Wilson and Hamilton, 1996]. We cannot

confidently identify any waves in this field. We do not present any figures for waves in the $m = 4$ T-average field owing to the low amplitudes and lack of discernable wave activity.

[42] There is little evidence of $s = 4$ stationary waves, with amplitudes typically < 1 K in low altitudes. Near northern fall equinox ($L_s = 135\text{--}195^\circ$), there is an area of $1\text{--}2$ K amplitude in the tropics and low latitudes with no clearly structured phase behavior (not shown).

[43] We also find little evidence of SK2. Perhaps this is to be expected given the expected low-temperature perturbation owing to SK2. However, we cannot connect a non-detection of significant amplitudes with a detection of SK2. Amplitudes of 1 K, to occasionally 2 K, are common in all seasons and latitude zones between 0.1 and 1 Pa (not shown). Were these associated with SK2, we would expect barotropic phase structures with altitude. However, eastward phase propagation of $30\text{--}40^\circ$ is typically observed with these maxima (not shown). Isolated latitude zones in particular seasons do have roughly barotropic phase profiles, but they are not associated with amplitudes > 1 K. These barotropic profiles are not constant between neighboring latitude zones.

3.8. T-Difference Field $m = 4$

[44] We expect DK3 to be the primary contributor to the $m = 4$ T-difference field with additional contribution from an $s = 5$, $\sigma = 1$ tide and possible higher-frequency (ter-diurnal) nonmigrating tides. DK3 and the $s = 5$, $\sigma = 1$ tide are forced by the interaction of the diurnal migrating tide with the $s = 4$ topography component. No previous unambiguous detections of DK3 have been made, but there has been some limited modeling work done on this wave [Wilson, 2000; Angelats i Coll et al., 2004]. DK3 is expected to be more confined to the tropics than either DK1 or DK2, with a shorter wavelength (50 km according to Wilson [2000]) and comparable amplitudes (~ 1 K). As described below, we report the first unambiguous detection of DK3 (see Figure 17 which covers the same equinoctial time period from $L_s 135\text{--}225^\circ$ as shown for DK1 and DK2).

[45] An amplitude structure very similar to the other Kelvin wave-dominated fields ($m = 2$ and $m = 3$ difference fields) is seen in the $m = 4$ T-difference field, with a low-

altitude maxima in the tropics, a dearth of amplitude between 5 and 100 Pa, and then generally increasing amplitude with height above (Figure 17a). Again the maximum amplitude is below the top of the observed domain, but very near 80 km altitude. DK3 is most obvious in data averaged around northern fall equinox ($L_s = 135\text{--}225$) when the amplitude structure is roughly symmetric about 5° N with a magnitude of 1–2 K and generally increases with height outside the near-surface maxima (Figure 17). Near the surface, the phase of the maximum is near 55° E and increases by 90° over the depth of the domain (Figure 17b). In the area between 5 and 100 Pa with weak amplitudes, the phase propagation is typically less coherent, suggesting influence of other waves. In northern winter ($L_s = 255\text{--}345$), when equatorial data are again available, amplitudes are weaker and do not exhibit the structure seen earlier in the year. The phase of the maximum is near 70° E with 110° of phase propagation over the domain (Figure 17b). Additional profiles from the tropics in other seasons corroborate these values, with average phase of the maximum near 60–65° E at the surface (not shown). The amount of phase propagation (90° is a full cycle for the $m = 4$ fields) suggests the vertical wavelength is closer to 100 km than 50 km, but we cannot confidently assign a value given the lack of consistency and noisy phase profiles in the 5–100 Pa range.

[46] From 25° S to 25° N the phase of the maximum is consistent (within the range of phase values given above) with DK3 year round throughout the vertical domain. Scattered profiles at higher latitudes (up to 50°) at different times of year also seem consistent with DK3, but there is less meridional consistency in neighboring profiles and higher variability in phase at a particular height. From $L_s = 45\text{--}105$ there is a 3 K amplitude maximum near 0.1 Pa over 40° N (not shown). Below this area, the phase is not consistent with DK3, but the phase near the maximum is consistent (to 10°) with the phase at this altitude over tropical latitudes from other times of the year associated with DK3.

[47] This field was also decomposed into symmetric and antisymmetric components. As with the $m = 3$ T-difference field, there was little or no amplitude associated with the antisymmetric field. The antisymmetric phase profiles near winter solstice do suggest a vertically propagating wave with a wavelength of 70–80 km (not shown). However, this is more than twice the wavelength of the lowest-order asymmetric eastward propagating wave number 3 diurnal Hough mode (35 km). Taken together, this result again implies that the symmetric Kelvin mode is dominating this field.

4. Conclusions

[48] We have analyzed waves in the Martian atmosphere using 35 months of atmospheric temperature profiles from MCS. In general, our results confirm and extend previous observations [e.g., Banfield et al., 2003] and modeling simulations [e.g., Wilson and Hamilton, 1996] of these waves.

[49] Features of the $s = 1$ stationary waves in the lower atmosphere were nearly identical to those seen previously [Hinson et al., 2003; Banfield et al., 2003] within the limits of our northern hemisphere data. A secondary temperature maxima in the vertical for the southern hemisphere stationary wave is observed that is not fully documented in

previous studies. The $s = 2$ stationary wave dominates at all observed altitudes and latitudes in the northern hemisphere and we confirm the $s = 1$ dominance of the southern hemisphere. We cannot confidently identify features associated with either the $s = 3$ or $s = 4$ stationary waves, most likely due to their limited vertical propagation in conjunction with sparse data in the lowest scale height of the atmosphere.

[50] We characterized diurnal Kelvin waves 1 through 3 (DK1, DK2, and DK3) and this is the first unambiguous detection of DK3. Both DK2 and DK3 appear to have longer wavelengths than what classical tidal theory calculates. Observed phase values and amplitudes for DK1 and DK2 closely match earlier studies, but isolated maxima of larger amplitudes also appear associated with these waves (5 K for DK1). DK1 is observed to have both symmetric and asymmetric modes contributing to the field. Additionally we identified the zonally symmetric diurnal tide and the semi-diurnal Kelvin wave 1 (SK1). Our analysis of the zonally symmetric diurnal tide yielded significant differences from previous studies with MGS TES that could potentially indicate interannual or seasonal variability or the presence of the westward $s = 2$ diurnal nonmigrating tide.

[51] Additional years of MCS data, including the expected flight of the ExoMars Climate Sounder in 2016, will hopefully yield an unprecedented record of the Martian atmosphere in space and time that will further illuminate its dynamics. In particular, the current data are limited near the equator and high latitudes, the precise areas most desirable for analyzing Kelvin waves and stationary planetary waves, respectively. Additional years of data collection by MCS should fill these holes. Many of the small-scale structure and features observed by MCS and partially described in this work require further analysis with data gathered by MCS in the future and its successors. General circulation modeling studies of higher wave number and higher period tides (many of which have shorter vertical wavelengths that get smoothed in MCS data collection), that have been aliased into these fields and might be responsible for some of these small-scale features, could also help describe the unidentified structures and features seen by MCS.

[52] **Acknowledgments.** This work was funded by a Johns Hopkins University Applied Physics Laboratory graduate student fellowship. E. R. Talaat was supported by National Science Foundation grant 0640864. The authors would also like to thank the MCS team for their efforts and timely submissions to the Planetary Data System.

References

- Angelats i Coll, M., F. Forget, M. A. López-Valverde, P. L. Read, and S. R. Lewis (2004), Upper atmosphere of Mars up to 120 km: Mars Global Surveyor accelerometer data analysis with the LMD general circulation model, *J. Geophys. Res.*, *109*, E01011, doi:10.1029/2003JE002163.
- Banfield, D., B. Conrath, J. C. Pearl, M. D. Smith, and P. Christensen (2000), Thermal tides and stationary waves on Mars as revealed by Mars Global Surveyor Thermal Emission Spectrometer, *J. Geophys. Res.*, *105*, 9521–9537, doi:10.1029/1999JE001161.
- Banfield, D., B. Conrath, M. D. Smith, and R. J. Wilson (2001), Mars transient and forced atmospheric waves from MGS TES: Climatology and interannual variability, *Bull. Am. Astron. Soc.*, *33*, 1067.
- Banfield, D., B. Conrath, M. D. Smith, P. R. Christensen, and R. J. Wilson (2003), Forced waves in the Martian atmosphere from MGS TES nadir data, *Icarus*, *161*, 319–345, doi:10.1016/S0019-1035(02)00044-1.
- Barnes, J. R., R. M. Haberle, J. B. Pollack, H. Lee, and J. Schaeffer (1996), Mars atmospheric dynamics as simulated by the NASA Ames general circulation model: 3. Winter quasi-stationary eddies, *J. Geophys. Res.*, *101*, 12,753–12,776, doi:10.1029/96JE00179.

- Bougher, S. W., S. Engel, D. P. Hinson, and J. M. Forbes (2001), Mars Global Surveyor radio science electron density profiles: Neutral atmosphere implications, *Geophys. Res. Lett.*, *28*, 3091–3094, doi:10.1029/2001GL012884.
- Bridger, A. F. C., and J. R. Murphy (1998), Mars' surface pressure tides and their behavior during global dust storms, *J. Geophys. Res.*, *103*, 8587–8601, doi:10.1029/98JE00242.
- Cahoy, K. L., D. P. Hinson, and G. L. Tyler (2006), Radio science measurements of atmospheric refractivity with Mars Global Surveyor, *J. Geophys. Res.*, *111*, E05003, doi:10.1029/2005JE002634.
- Chapman, S., and R. S. Lindzen (1970), *Atmospheric Tides*, D. Reidel, Norwell, Mass.
- Conrath, B. J. (1976), Influence of planetary-scale topography on the diurnal thermal tide during the 1971 Martian dust storm, *J. Atmos. Sci.*, *33*, 2430–2439, doi:10.1175/1520-0469(1976)033<2430:IOPSTO>2.0.CO;2.
- Conrath, B. J. (1981), Planetary-scale wave structure in the Martian atmosphere, *Icarus*, *48*, 246–255, doi:10.1016/0019-1035(81)90107-X.
- Forbes, J. M., and M. E. Hagan (2000), Diurnal kelvin wave in the atmosphere of Mars: Towards an understanding of “stationary” density structures observed by the MGS accelerometer, *Geophys. Res. Lett.*, *27*, 3563–3566, doi:10.1029/2000GL011850.
- Forbes, J. M., A. F. C. Bridger, S. W. Bougher, M. E. Hagan, J. L. Hollingsworth, G. M. Keating, and J. Murphy (2002), Nonmigrating tides in the thermosphere of Mars, *J. Geophys. Res.*, *107*(E11), 5113, doi:10.1029/2001JE001582.
- Forget, F., F. Montmessin, J.-L. Bertaux, F. González-Galindo, S. Lebonnois, E. Quémerais, A. Reberac, E. Dimarellis, and M. A. López-Valverde (2009), Density and temperatures of the upper Martian atmosphere measured by stellar occultations with Mars Express SPICAM, *J. Geophys. Res.*, *114*, E01004, doi:10.1029/2008JE003086.
- Heavens, N. G., D. J. McCleese, M. I. Richardson, D. M. Kass, A. Kleinböhl, and J. T. Schofield (2011a), Structure and dynamics of the Martian lower and middle atmosphere as observed by the Mars Climate Sounder: 2. Implications of the thermal structure and aerosol distributions for the mean meridional circulation, *J. Geophys. Res.*, *116*, E01010, doi:10.1029/2010JE003713.
- Heavens, N. G., M. I. Richardson, A. Kleinböhl, D. M. Kass, D. J. McCleese, W. Abdou, J. L. Benson, J. T. Schofield, J. H. Shirley, and P. M. Wolkenberg (2011b), Vertical distribution of dust in the Martian atmosphere during northern spring and summer: High-altitude tropical dust maximum at northern summer solstice, *J. Geophys. Res.*, *116*, E01007, doi:10.1029/2010JE003692.
- Hess, S. L., R. M. Henry, C. B. Leovy, J. A. Ryan, and J. E. Tillman (1977), Meteorological results from the surface of Mars: Viking 1 and 2, *J. Geophys. Res.*, *82*, 4559–4574, doi:10.1029/JS082i028p04559.
- Hinson, D., and R. J. Wilson (2004), Temperature inversions, thermal tides, and water ice clouds in the Martian tropics, *J. Geophys. Res.*, *109*, E01002, doi:10.1029/2003JE002129.
- Hinson, D., G. Tyler, J. Hollingsworth, and R. Wilson (2001), Radio occultation measurements of forced atmospheric waves on Mars, *J. Geophys. Res.*, *106*, 1463–1480, doi:10.1029/2000JE001291.
- Hinson, D., R. J. Wilson, M. D. Smith, and B. J. Conrath (2003), Stationary planetary waves in the atmosphere of Mars during southern winter, *J. Geophys. Res.*, *108*(E1), 5004, doi:10.1029/2002JE001949.
- Hinson, D., M. Patzold, R. J. Wilson, B. Hausler, S. Tellmann, and G. L. Tyler (2008), Radio occultation measurements and MGCM simulations of Kelvin waves on Mars, *Icarus*, *193*, 125–138, doi:10.1016/j.icarus.2007.09.009.
- Hollingsworth, J. L., and J. R. Barnes (1996), Forced stationary planetary waves in Mars's winter atmosphere, *J. Atmos. Sci.*, *53*, 428–448, doi:10.1175/1520-0469(1996)053<0428:FSPWIM>2.0.CO;2.
- Keating, G. M., et al. (1998), The structure of the upper atmosphere of Mars: In situ accelerometer measurements from Mars Global Surveyor, *Science*, *279*, 1672–1676, doi:10.1126/science.279.5357.1672.
- Kleinböhl, A., et al. (2009), Mars Climate Sounder limb profile retrieval of atmospheric temperature, pressure, and dust and water ice opacity, *J. Geophys. Res.*, *114*, E10006, doi:10.1029/2009JE003358.
- Lee, C., et al. (2009), Thermal tides in the Martian middle atmosphere as seen by the Mars Climate Sounder, *J. Geophys. Res.*, *114*, E03005, doi:10.1029/2008JE003285.
- Leovy, C. B. (1981), Observations of Martian tides over two annual cycles, *J. Atmos. Sci.*, *38*, 30–39, doi:10.1175/1520-0469(1981)038<0030:OOMTOT>2.0.CO;2.
- Leovy, C. B., and R. W. Zurek (1979), Thermal tides and Martian dust storms: Direct evidence for coupling, *J. Geophys. Res.*, *84*, 2956–2968, doi:10.1029/JB084iB06p02956.
- Lewis, S. R., and P. R. Barker (2005), Atmospheric tides in a Mars general circulation model with data assimilation, *Adv. Space Res.*, *36*, 2162–2168, doi:10.1016/j.asr.2005.05.122.
- Lieberman, R. S. (1991), Nonmigrating diurnal tides in the equatorial middle atmosphere, *J. Atmos. Sci.*, *48*, 1112–1123, doi:10.1175/1520-0469(1991)048<1112:NDTITE>2.0.CO;2.
- Lieberman, R. S., J. Oberheide, M. E. Hagan, E. E. Remsberg, and L. L. Gordley (2004), Variability of diurnal tides and planetary waves during November 1978–May 1979, *J. Atmos. Sol. Terr. Phys.*, *66*, 517–528, doi:10.1016/j.jastp.2004.01.006.
- Longuet-Higgins, M. S. (1968), The eigenfunctions of Laplace's tidal equations over a sphere, *Philos. Trans. R. Soc. London, Ser. A*, *262*, 511–607, doi:10.1098/rsta.1968.0003.
- Martin, T. Z. (1981), Mean thermal and albedo behavior of the Mars surface and atmosphere over a Martian year, *Icarus*, *45*, 427–446, doi:10.1016/0019-1035(81)90045-2.
- McCleese, D. J., J. T. Schofield, F. W. Taylor, S. B. Calcutt, M. C. Foote, D. M. Kass, C. B. Leovy, D. A. Paige, P. L. Read, and R. W. Zurek (2007), Mars Climate Sounder: An investigation of thermal and water vapor structure, dust and condensate distributions in the atmosphere, and energy balance of the polar regions, *J. Geophys. Res.*, *112*, E05S06, doi:10.1029/2006JE002790.
- McCleese, D. J., et al. (2010), Structure and dynamics of the Martian lower and middle atmosphere as observed by the Mars Climate Sounder: Seasonal variations in zonal mean temperature, dust, and water ice aerosols, *J. Geophys. Res.*, *115*, E12016, doi:10.1029/2010JE003677.
- Oberheide, J., M. E. Hagan, R. G. Roble, and D. Offermann (2002), Sources of nonmigrating tides in the tropical middle atmosphere, *J. Geophys. Res.*, *107*(D21), 4567, doi:10.1029/2002JD002220.
- Richardson, M. I., A. D. Toigo, and C. E. Newman (2007), PlanetWRF: A general purpose, local to global numerical model for planetary atmospheric and climate dynamics, *J. Geophys. Res.*, *112*, E09001, doi:10.1029/2006JE002825.
- Salby, M. L. (1982), Sampling theory for synoptic satellite observations. Part I: Space-time spectra, resolution, and aliasing, *J. Atmos. Sci.*, *39*, 2577–2600, doi:10.1175/1520-0469(1982)039<2577:STFASO>2.0.CO;2.
- Smith, M. D., J. C. Pearl, B. J. Conrath, and P. R. Christensen (2001), Thermal Emission Spectrometer results: Mars atmospheric thermal structure and aerosol distribution, *J. Geophys. Res.*, *106*, 23,929–23,945, doi:10.1029/2000JE001321.
- Talaat, E. R., and R. S. Lieberman (1999), Nonmigrating diurnal tides in mesospheric and lower thermospheric winds and temperatures, *J. Atmos. Sci.*, *56*, 4073–4087, doi:10.1175/1520-0469(1999)056<4073:NDTIMA>2.0.CO;2.
- Wilson, R. J. (2000), Evidence for diurnal period kelvin waves in the Martian atmosphere from Mars Global Surveyor TES data, *Geophys. Res. Lett.*, *27*, 3889–3892, doi:10.1029/2000GL012028.
- Wilson, R. J. (2002), Evidence for nonmigrating thermal tides in the Mars upper atmosphere from the Mars Global Surveyor Accelerometer Experiment, *Geophys. Res. Lett.*, *29*(7), 1120, doi:10.1029/2001GL013975.
- Wilson, R. J., and K. Hamilton (1996), Comprehensive model simulation of thermal tides in the Martian atmosphere, *J. Atmos. Sci.*, *53*, 1290–1326, doi:10.1175/1520-0469(1996)053<1290:CMSOTT>2.0.CO;2.
- Wilson, R. J., and M. I. Richardson (2000), The Martian atmosphere during the Viking Mission, I: Infrared measurements of atmospheric temperatures revisited, *Icarus*, *145*, 555–579, doi:10.1006/icar.2000.6378.
- Withers, P., and D. C. Catling (2010), Observations of atmospheric tides on Mars at the season and latitude of the Phoenix atmospheric entry, *Geophys. Res. Lett.*, *37*, L24204, doi:10.1029/2010GL045382.
- Withers, P., S. W. Bougher, and G. M. Keating (2003), The effects of topographically controlled thermal tides in the Martian upper atmosphere as seen by the MGS accelerometer, *Icarus*, *164*, 14–32, doi:10.1016/S0019-1035(03)00135-0.
- Zurek, R. (1976), Diurnal tide in the Martian atmosphere, *J. Atmos. Sci.*, *33*, 321–337, doi:10.1175/1520-0469(1976)033<0321:DTITMA>2.0.CO;2.
- Zurek, R. (1988), Free and forced modes in the Martian atmosphere, *J. Geophys. Res.*, *93*, 9452–9462, doi:10.1029/JD093iD08p09452.
- Zurek, R., and C. B. Leovy (1981), Thermal tides in the dusty Martian atmosphere: A verification of theory, *Science*, *213*, 437–439, doi:10.1126/science.213.4506.437.
- Zurek, R., J. R. Barnes, R. M. Haberle, J. B. Pollack, J. E. Tillman, and C. B. Leovy (1992), Dynamics of the atmosphere of Mars, in *Mars*, edited by H. H. Kieffer et al., pp. 835–933, Univ. of Ariz. Press, Tucson.

S. D. Guzewich and D. W. Waugh, Department of Earth and Planetary Sciences, Johns Hopkins University, 3400 N. Charles St., 301 Olin Hall, Baltimore, MD 21218, USA. (guzewich@jhu.edu)

E. R. Talaat, Johns Hopkins University Applied Physics Laboratory, 11100 Johns Hopkins Rd., Laurel, MD 20723, USA.